Available online at www.sciencedirect.com

ScienceDirect

Journal of Computational Physics 227 (2007) 919–945

JOURNAL OF
COMPUTATIONAL
PHYSICS

www.elsevier.com/locate/jcp

Fourier spectral and wavelet solvers for the incompressible Navier–Stokes equations with volume-penalization: Convergence of a dipole–wall collision

G.H. Keetels [a,*], U. D'Ortona [c], W. Kramer [a], H.J.H. Clercx [a,b], K. Schneider [c,d], G.J.F. van Heijst [a]

[a] *Department of Physics, Eindhoven University of Technology, P.O. Box 513, 5600 MB Eindhoven, The Netherlands*
[b] *Department of Applied Mathematics, University of Twente, P.O. Box 217, 7500 AE Enschede, The Netherlands*
[c] *Laboratoire de Modèlisation et Simulation Numèrique en Mècanique et Gènie des Procèdès,*
CNRS and Universitès d'Aix-Marseille, 38 rue F. Joliot-Curie, 13451 Marseille Cedex 20, France
[d] *Centre de Mathèmatiques et d'Informatique, Universitè de Provence, 39 rue F. Joliot-Curie 13453 Marseille Cedex 13, France*

Received 23 December 2006; received in revised form 10 July 2007; accepted 27 July 2007
Available online 31 August 2007

Abstract

In this study, we use volume-penalization to mimic the presence of obstacles in a flow or a domain with no-slip boundaries. This allows in principle the use of fast Fourier spectral methods and coherent vortex simulation techniques (based on wavelet decomposition of the flow variables) to compute turbulent wall-bounded flow or flows around solid obstacles by simply adding one term in the equation. Convergence checks are reported using a recently revived, and unexpectedly difficult dipole–wall collision as a benchmark computation. Several quantities, like the vorticity isolines, truncation error, kinetic energy and enstrophy are inspected for a collision of a dipole with a no-slip wall and compared with available benchmark data obtained with a standard Chebyshev pseudospectral method. We quantify the possible deteriorating effects of the Gibbs phenomenon present in the Fourier based schemes due to continuity restrictions of the penalized Navier–Stokes equations on the wall. It is found that Gibbs oscillations have a negligible effect on the flow evolution allowing higher-order recovery of the accuracy on a Fourier basis by means of postprocessing. An advantage of coherent vortex simulations, on the other hand, is that the degrees of freedom of the flow computation can strongly be reduced. In this study, we quantify the possible reduction of degrees of freedom while keeping the accuracy. For an optimal convergence scenario the penalization parameter has to scale with the number of Fourier and wavelet modes. In addition, an implicit treatment of the Darcy drag term in the penalized Navier–Stokes equations is beneficial since this allows one to set the time step independent from the penalization parameter without additional computational or memory requirements.

Keywords: Immersed boundary; Two-dimensional turbulence; Volume-penalization; Spectral methods; Wavelets; Coherent vortex simulation (CVS)

---

[*] Corresponding author.
E-mail address: g.h.keetels@tue.nl (G.H. Keetels).

0021-9991/$ - see front matter © 2007 Elsevier Inc. All rights reserved.
doi:10.1016/j.jcp.2007.07.036

1. Introduction

A simple two-dimensional vortex–wall collision poses a serious challenge for CFD methods, see, for example, the simulation of the dipole–wall collision with a no-slip wall conducted with both finite differences and Chebyshev spectral methods [6]. In particular, the formation and detachment of very thin boundary layers, containing high-amplitude vorticity, during the collision process and the subsequent formation of small-scale vorticity patches in the near-wall region can possibly deteriorate the accuracy of the flow computation. This dramatically affects the dynamics of the flow after the impact. The initial flow field fulfills the boundary condition (within machine precision no normal and tangential velocities at the no-slip boundaries) such that initialization errors are avoided. The boundary layers are produced during the approach of the dipole to the wall. The production of small-scale vorticity during the vortex–wall interaction makes this process a very good benchmark for many CFD methods aimed at simulation of wall-bounded flows or flows around solid obstacles.

The first numerical investigation of the dipole–wall problem was conducted by Orlandi [30] already a decade ago. Later, other studies used the dipole–wall collision experiment to investigate the reliability of several CFD methods. For example, Ould-Salihi et al. [31] used this test case to validate particle methods against finite-difference methods. Cottet et al. [10,11] used the dipole–wall collision as a benchmark to validate mesh adaption techniques that allow the use of refined vortex methods in both directions near the wall. Another example, considering a B-spline numerical method, can be found in Kravchenko et al. [26]. They analyzed the effect of zonal embedded grids on the evolution of the dipole–wall collision. Clercx and Bruneau [6] provide, on the other hand, a more detailed comparison of finite differences and a pseudo-spectral Chebyshev method. It was observed that the dipole–wall problem is an extremely though test case, i.e. the resolution to achieve grid or mode convergence should be substantially larger than considered previously.

In this paper, we examine the convergence and accuracy of a fast Fourier spectral method combined with an immersed boundary technique called volume-penalization [1] to mimic the no-slip boundary condition. Fourier spectral methods are potentially accurate for sufficiently smooth functions on double-periodic domains. Moreover, these methods are fast, relatively easy to implement even for performing parallel computations (see Ref. [41]). Incorporation of no-slip boundaries is, however, not straightforward.

In the volume-penalization approach of Arquis and Caltagirone [2] a Darcy drag term is added to the Navier–Stokes equations such that the velocity is penalized towards zero inside an obstacle. It is analytically shown that by increasing the penalization strength the penalized Navier–Stokes equations converge towards the Navier–Stokes equations with no-slip boundary conditions (see Refs. [1,5]). Angot and co-workers [1] also present numerical results for 2D flow around a square obstacle, which confirms that the method is indeed converging. The maximum value of the Reynolds number in their simulations, based on the main stream velocity U_0, the size of the square L, and the kinematic viscosity ν, is $Re = \frac{U_0 L}{\nu} = 80$, which is relatively low. Paccou et al. [33] also proved numerically and theoretically convergence of a volume-penalization approach for a fully hyperbolic problem, i.e. the linear wave equation.

Kevlahan and Ghidaglia [24] tested the suitability of a Fourier spectral scheme with volume-penalization for the problem of flow around a cylinder at a substantially higher Reynolds number, $Re = \frac{U_0 D}{\nu} = 1000$, based on the main stream velocity and the diameter D of the cylinder. A drawback of the penalization technique is the formation of steep velocity-gradients inside the porous object, that can deteriorate the spectral convergence rate to first order. This effect is generally referred to as the Gibbs phenomenon, visibly present by wiggles in both the Fourier Galerkin and collocation projection of any piecewise continuous function. Nevertheless, the Gibbs oscillations present in the simulations of Kevlahan and Ghidaglia [24] and Schneider [34] seem to be stable during the flow evolution. This demonstrates that it is possible to perform stable and reasonably accurate Fourier spectral computations of incompressible viscous flow past an arbitrary shaped object. We think it is interesting to extend this analysis using the very challenging dipole–wall collision experiment at high Reynolds numbers as a test problem. An important issue is to fully quantify the role of the Gibbs effect on the flow dynamics: is it possible to recover higher-order accuracy of the Fourier spectral scheme? Here, we follow some recent developments in the theory and application of Fourier spectral methods on discontinuous phenomena, see for an overview the work of Gottlieb and Gottlieb [18]. These advances indicate that high-order information can be recovered from stable Fourier spectral computations. We use a high-order recovery technique proposed by Tadmor and Tanner [40]. They propose a mollification procedure, which involves a subtle process of cancelling nearby Gibbs oscillations to obtain an accurate reconstruction of any piecewise continuous function in the physical domain. A strong advantage is that tuning of the parameters is completely avoided. Furthermore, the implementation is quite straightforward and thus relatively easy to optimize from a computational point of view.

Besides the Fourier spectral technique we will consider the coherent vortex simulation (CVS) method with volume-penalization using an adaptive wavelet method. The main idea is to split the flow into two orthogonal parts, a coherent contribution and an incoherent background flow, using a nonlinear wavelet filtering of vorticity [15]. It is shown by Beta et al. [3] that the coherent part is mainly responsible for the nonlinear dynamics, while the incoherent background can be considered as decorrelated or structureless. Therefore, Farge and Schneider [16] propose to model its influence on the coherent flow statistically and only solve by direct numerical simulation the few wavelets coefficients that describe the coherent part of the flow. This makes the CVS method potentially fast in terms of CPU time, while the memory requirements can strongly be reduced. Schneider and Farge successfully applied the CVS method to different flow problems such as flow around a cylinder [36], 3D turbulent mixing layers [37,38] and present some preliminary results (containing aliasing errors) for a dipole–wall collision [35].

In this paper, we will continue with a more detailed comparison of the CVS and Fourier spectral results with a high-resolution benchmark computation conducted with a Chebyshev–Fourier and Chebyshev spectral method for 2D flow with no-slip boundary conditions in one or two directions, respectively (see Refs. [25,8]). We start with a description of the volume-penalization technique and formulate different approaches to treat the Darcy drag term in Fourier spectral schemes and in CVS. Then the convergence of these schemes and the penalization error will be analyzed in terms of isovorticity lines, a global measure of the error in the vorticity and the total kinetic energy and enstrophy of the flow.

2. Volume-penalization

2.1. The model equation

Consider an incompressible fluid of unit density, $\rho = 1$, in a domain $\Omega_{\mathrm{f}} \in \mathbb{R}^2$, which evolves according to the Navier–Stokes equations

$$\partial_t \mathbf{u} + (\mathbf{u} \cdot \nabla)\mathbf{u} + \nabla p - \nu \Delta \mathbf{u} = 0 \quad \text{in } \Omega_{\mathrm{f}} \times [0, T] \tag{1}$$

and the continuity condition

$$\nabla \cdot \mathbf{u} = 0 \quad \text{in } \Omega_{\mathrm{f}} \times [0, T], \tag{2}$$

where $\mathbf{u} = (u(\mathbf{x}, t), v(\mathbf{x}, t))$ is the Eulerian velocity, $p = p(\mathbf{x}, t)$ the scalar kinetic pressure and ν the kinematic viscosity. An impermeable, stationary geometry can be defined by setting the normal velocity component to the wall to zero. The tendency of a fluid to stick to the boundaries $\partial\Omega_{\mathrm{f}}$ is usually modelled by removing the tangential velocity component relative to the wall. The combination of these boundary conditions on each component of the velocity defines the no-slip boundary condition, which read for a stationary geometry,

$$\mathbf{u}(\mathbf{x}, t) = 0, \quad \mathbf{x} \in \partial\Omega_{\mathrm{f}}, \quad t \in [0, T], \tag{3}$$

which is essentially a Dirichlet boundary condition for $\mathbf{u}$. Note that Eq. (1) contains second-order derivatives so two boundary conditions are required for the existence of a unique solution.

In the volume-penalization approach fluid–wall interaction is no longer described by demanding the no-slip boundary condition (3). The basic idea originating from Arquis and Caltagirone [2] is to embed the flow domain in a larger domain Ω, such that $\Omega_{\mathrm{f}} = \Omega \setminus \overline{\Omega_{\mathrm{s}}}$, where Ω_{s} represents the volume of porous objects. The interaction with the porous objects is modelled by adding a Darcy drag term to the Navier–Stokes equations locally inside Ω_s, which yields the penalized Navier–Stokes equations

$$\partial_t \mathbf{u} + (\mathbf{u} \cdot \nabla)\mathbf{u} + \nabla p - \nu \Delta \mathbf{u} + \frac{1}{\epsilon} H \mathbf{u} = 0 \quad \text{in } \Omega \times [0, T], \tag{4}$$

where the mask function H is defined as

$$H = \begin{cases} 1 & \text{if } \mathbf{x} \in \overline{\Omega}_{\mathrm{s}}, \\ 0 & \text{if } \mathbf{x} \in \Omega_{\mathrm{f}}. \end{cases}$$

Fig. 1 shows some examples of possible geometries. In this study, we model a channel with two no-slip boundaries and two periodic boundaries and the square bounded geometry with four no-slip boundaries by choosing the mask function shown in Fig. 1b and c, respectively. The continuity condition accompanies the penalized Navier–Stokes equations in Ω. On the boundaries of the computational domain $\partial\Omega$ one can consider different boundary conditions. Here, we have chosen for the periodic boundary condition on $\partial\Omega$, such that Fourier spectral methods can be applied. For convenience the penalized Navier–Stokes equation (4) can be rewritten in velocity–vorticity formulation by taking the curl of Eq. (4) and applying several vector identities to arrive at

$$\partial_t \omega + (\mathbf{u} \cdot \nabla)\omega - \nu\Delta\omega + \frac{1}{\epsilon}\nabla \times H\mathbf{u} = 0 \quad \text{in } \Omega \times [0, T], \tag{5}$$

where $\omega = (\nabla \times \mathbf{u}) \cdot \mathbf{e}_z$ is the vorticity. Note that the velocity–vorticity formulation is scalar-valued in two dimensions. The volume of the obstacles can be interpreted as a porous medium with permeability ϵ. As a consequence the flow inside Ω_{f} induces a small and time-dependent velocity inside the obstacles and thus on the boundaries $\partial\Omega_{\mathrm{s}}$. The flow inside the obstacle Ω_{s} can be matched with the flow inside Ω_{f} by demanding continuity of both velocity and surface stress. Note that Darcy drag can be considered as a volume force such that the surface stresses $\boldsymbol{\tau}$ in the penalized Navier–Stokes equation (4) can be expressed in the usual way, i.e. $\boldsymbol{\tau} = \boldsymbol{n} \cdot \boldsymbol{\sigma}$, where $\boldsymbol{n}$ is the outward unit normal on $\partial\Omega_{\mathrm{s}}$ and the stress tensor $\boldsymbol{\sigma} = \nu(\nabla u + \nabla u^t) - p\boldsymbol{I}$. This implies together with demanding continuity that the velocity is at least C^1 and the pressure C^0 on $\partial\Omega_{\mathrm{s}}$ (see Ref. [5]).

2.2. Convergence and regularity

It has been shown rigorously by Angot et al. [1] that the solutions of the penalized Navier–Stokes equations converge towards the Navier–Stokes solution in Ω_{f} with an order $\epsilon^{1/4}$ error bound. Their numerical simulations show, however, a better convergence indicating that the analytical upper bound for the error is not sharp enough. Later, Carbou and Fabrie [5] improved the analytical error estimate inside the flow domain by using a singular perturbation technique. They obtained formal expansions for the velocity and pressure in terms of $\sqrt{\epsilon}$ inside Ω. In addition, they derived that the upper bound of the penalization error is order $\sqrt{\epsilon}$ in the L_2 sense of the velocity and velocity gradients with respect to the Navier–Stokes solution in Ω_{f} with the no-slip boundary condition. Furthermore, they found C^1 continuity in the larger domain Ω of the velocities determined by the penalized Navier–Stokes equations. The C^1 continuity of the $\sqrt{\epsilon}$ and higher-order expansion terms is achieved by the introduction of an asymptotically thin boundary layer proportional to $\sqrt{\nu\epsilon}$ inside the obstacle.

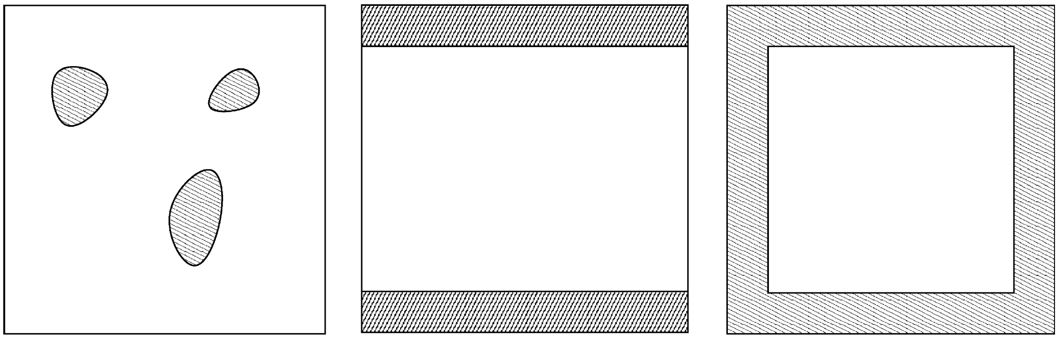

(a) obstacles (b) channel (c) square

Fig. 1. Decomposition of a square computational domain Ω into porous objects Ω_{s} (dashed) and flow domain Ω_{f} (white).

A remarkable result is, however, that the boundary layer components are only required to determine the order ϵ and higher-order terms in the asymptotic expansion of the velocity and pressure inside Ω_{f}. Therefore, it might be expected that if the spatial resolution is too low to resolve the details of the asymptotic boundary layer, one is still able to compute the solution of the penalized Navier–Stokes equations in Ω_{f} up to order $\sqrt{\epsilon}$ accurate. Inside the obstacles ($\mathrm{dist}(x, \partial\Omega_{\mathrm{s}}) \gg \sqrt{\nu\epsilon}$) the leading order expansion term for the velocity is order ϵ and for the pressure order zero. These terms can uniquely be determined, again without computing the boundary layer solution. The zeroth-order part of the pressure follows a Laplace equation that can be solved by applying a matching condition on $\partial\Omega_{\mathrm{s}}$. The order ϵ part of the velocity can then be determined by solving a Darcy relation involving the zeroth-order part of the pressure. An advantage of the small skin depth is, on the other hand, that the obstacles can be relatively thin. This implies that not many grid points are required to represent a wall on a Cartesian grid and for adaptive methods, such as CVS, only the flow near the surface of the porous objects needs to be calculated.

3. Numerical methods

In this section, we present an overview of the different numerical schemes.

3.1. Fourier–Galerkin method with an explicit treatment of Darcy drag

For the sake of simplicity, we write Eq. (5) as

$$\partial_t\omega - \nu\Delta\omega = \mathcal{N}(\omega), \tag{6}$$

where

$$\mathcal{N} = -(\mathbf{u}\cdot\nabla)\omega - \frac{1}{\epsilon}\nabla\times H\mathbf{u}.$$

For the exact treatment of the diffusion term, we first consider the homogeneous equation, i.e., $\mathcal{N} = 0$. The exact solution can be expressed as

$$\omega(\boldsymbol{x}, t) = \omega(\boldsymbol{x}, t_0)\exp(\nu t\Delta), \tag{7}$$

where $\exp(\nu t\Delta)$ is the semi-group of the heat-kernel. By using variation of constants the inhomogeneous equation, i.e., $\mathcal{N} \neq 0$ can be written in the form

$$\partial_t\{\omega\exp(-\nu t\Delta)\} = \mathcal{N}(\omega)\exp(-\nu t\Delta), \tag{8}$$

See e.g., Ref. [34] for details. The vorticity and velocity are expanded with a doubly truncated Fourier series as a trial basis,

$$\omega_N(\boldsymbol{x}, t) = \sum_{k_x=-N/2}^{N/2-1}\sum_{k_y=-N/2}^{N/2-1}\hat{\omega}_{\boldsymbol{k}}(t)\exp(\mathrm{i}\boldsymbol{k}\cdot\boldsymbol{x}), \tag{9}$$

where $\boldsymbol{k} = (k_x, k_y)$ and $\hat{\omega}_{\boldsymbol{k}}(t)$ denotes the continuous Fourier expansion coefficients of $\omega(\boldsymbol{x}, t)$, which are defined for simplicity on $\boldsymbol{x} \in [0, 2\pi]^2$ as

$$\hat{\omega}_{\boldsymbol{k}}(t) = \frac{1}{4\pi^2}\int\omega(\boldsymbol{x}, t)\exp(-\mathrm{i}\boldsymbol{k}\cdot\boldsymbol{x})\mathrm{d}\boldsymbol{x}. \tag{10}$$

Note that the trigonometric polynomials are complete for functions in $L_2(\Omega)$. Thus it is, in principle, possible to make an expansion of functions with Dirichlet boundary conditions on $\partial\Omega$ as well. However, the convergence of the Fourier series expansion is only guaranteed in the L_2-norm and not in the pointwise sense. Note that setting a Dirichlet boundary condition actually requires convergence in the pointwise sense. Therefore, it is not possible to directly take into account the Dirichlet boundary condition on the domain boundaries. One thus has to apply immersed boundary techniques like, for example, the volume-penalization method in this study and consider periodic boundary conditions.

By virtue of the continuity condition (2) the velocity $\hat{\mathbf{u}}_{\boldsymbol{k}}(t)$ can be computed from $\hat{\omega}_{\boldsymbol{k}}(t)$,

$$\hat{\mathbf{u}}_{\boldsymbol{k}}(t) = \frac{\mathrm{i}(k_y \boldsymbol{e}_x - k_x \boldsymbol{e}_y)}{k^2} \hat{\omega}_{\boldsymbol{k}}(t), \tag{11}$$

where $k^2 = \boldsymbol{k} \cdot \boldsymbol{k}$. By substitution of the expansions into Eq. (8) and taking inner products with the Fourier system as test functions as well, we follow a Fourier–Galerkin approach yielding an evolution equation for each $\boldsymbol{k}$

$$d_t\{\hat{\omega}_{\boldsymbol{k}} \exp(\nu k^2 t)\} = \mathcal{K}(\hat{\omega}_{\boldsymbol{k}}) \exp(\nu k^2 t), \tag{12}$$

where

$$\mathcal{K} = [(\mathbf{u}_N \cdot \nabla)\omega_N]_{\boldsymbol{k}} + \frac{\mathrm{i}k_x}{\epsilon}[Hv_N]_{\boldsymbol{k}} - \frac{\mathrm{i}k_y}{\epsilon}[Hu_N]_{\boldsymbol{k}}. \tag{13}$$

This $\mathcal{K}$ term is evaluated by collocation in the physical domain where aliasing is avoided by applying the zero-padding technique introduced by Orszag [32], generally referred to as the 2/3-rule (see, for details, Ref. [4]). Furthermore, it is important to realize that in the Fourier–Galerkin approach the precise form of the continuous equation in this case the velocity–pressure (4) and velocity–vorticity (5) formulation yield identical algorithms. The computation of $\mathcal{K}$ involves Fourier projections of the discontinuous restricted velocities Hu and Hv, which might affect the convergence of the scheme.

A third-order extrapolated backward differentiation (BDF3) formula [22] is applied for the time discretization of Eq. (12)

$$\sum_{h=0}^{3} \alpha_h \hat{\omega}_{\boldsymbol{k}}^{n+1-h} \exp(-\nu k^2 h \delta t) = -\delta t \sum_{h=1}^{3} \beta_h \mathcal{K}(\hat{\omega}_{\boldsymbol{k}}^{n+1-h}) \exp(-\nu k^2 h \delta t). \tag{14}$$

The values of the coefficients α_h and β_h, which can be found in Table 1, are given by the backward differentiation scheme and extrapolation, respectively. We chose this time scheme for the good stability results obtained by Kress and Löstedt [27]. They considered backward difference time schemes with fourth-order finite differences for the spatial discretization of the incompressible Navier–Stokes equations with no-slip boundaries in a straight channel. Note that the treatment of viscous diffusion in Eq. (14) is exact. The accuracy and stability restrictions of the time scheme solely arise from the nonlinear $\mathcal{K}$ term.

3.2. Fourier collocation with an implicit treatment of Darcy drag

A drawback of the explicit treatment of the Darcy drag is that for stability the time step has to be of the same order as ϵ, because the problem is stiff. Recall that the accuracy of the penalized Navier–Stokes equations with respect to the no-slip boundary condition converges relatively slow with order $\sqrt{\epsilon}$. Therefore, it might be necessary to decouple the time step from ϵ, such that the time step is only limited by the CFL number. Kevlahan and Ghidaglia [24] used a GMRES Krylov subspace technique in an explicit time scheme for this purpose. To achieve a stiffly stable third-order time scheme, without additional memory or computational requirements we consider an alternative method. It is based on a collocation approach of the penalized Navier–Stokes equations in primitive variables (4) at the grid points $\boldsymbol{x} = (2\pi n_x/N, 2\pi n_y/N)$ where n_x and n_y range from $0, \ldots, N-1$. The grid values of $\boldsymbol{u}_N$ and p_N are now related to the discrete Fourier coefficients defined as

$$\tilde{p}_{\boldsymbol{k}} = \frac{1}{N^2} \sum_{n_x=0}^{N-1} \sum_{n_y=0}^{N-1} p_N(\boldsymbol{x}) \exp(-\mathrm{i}\boldsymbol{k} \cdot \boldsymbol{x}) \tag{15}$$

Table 1
Coefficients for third-order extrapolated backward differentiation (BDF3)

α_0	α_1	α_2	α_3	β_1	β_2	β_3
11/6	−3	3/2	−1/3	3	−3	1

such that

$$p_N(\boldsymbol{x}) = \sum_{k_x=-N/2}^{N/2-1} \sum_{k_y=-N/2}^{N/2-1} \tilde{p}_{\boldsymbol{k}} \exp(\mathrm{i}\boldsymbol{k}\cdot\boldsymbol{x}) \tag{16}$$

due to the orthogonality of the Fourier basis. A third-order extrapolated BDF scheme with exact differentiation of the diffusion term can be expressed as

$$\alpha_0 \boldsymbol{u}_N^{n+1} + \delta t \boldsymbol{L}_N(\boldsymbol{u}_N^{n+1}) = -\sum_{h=1}^{3} \left(\delta t \beta_h \boldsymbol{G}_N(\boldsymbol{u}_N^{n+1-h}) + \alpha_h \boldsymbol{u}_N^{n+1-h}\right) \mathrm{e}^{h\delta t \nu \Delta} \tag{17}$$

$$\widetilde{\nabla}\cdot \boldsymbol{u}_N = 0 \tag{18}$$

where $\boldsymbol{G}_N = (\boldsymbol{u}_N\cdot\widetilde{\nabla})\boldsymbol{u}_N + \widetilde{\nabla} p_N$, $\boldsymbol{L}_N = \frac{1}{\epsilon} H \boldsymbol{u}_N$ and a tilde stresses that collocation derivatives are used. The same values of the coefficients α_j and β_j are applied as for the explicit time scheme, see Table 1. Thus, the Darcy drag is now evaluated with backward differentiation instead of extrapolation. The error $\widetilde{\nabla} u - (\nabla u)_N$ is of the same order as the truncation error of the Fourier–Galerkin derivative of u (see Ref. [4]). In the following, we will neglect this error and suppose that interpolation and differentiation commute, i.e., $\widetilde{\nabla} u = (\nabla u)_N$ for simplicity. To keep the velocity field solenoidal with respect to the collocation derivatives we demand,

$$\widetilde{\nabla}\cdot \boldsymbol{G}_N = 0, \tag{19}$$

such that the Helmholtz decomposition of $\boldsymbol{G}_N$ only contains a rotational part,

$$\boldsymbol{G}_N = \widetilde{\nabla}\times \boldsymbol{A}. \tag{20}$$

Taking the curl on both sides of Eq. (20) yields,

$$\widetilde{\nabla}\times[(\boldsymbol{u}_N\cdot\widetilde{\nabla})\boldsymbol{u}_N] = \widetilde{\nabla}\times(\widetilde{\nabla}\times\boldsymbol{A}) = \widetilde{\nabla}(\widetilde{\nabla}\cdot\boldsymbol{A}) - \widetilde{\nabla}^2\boldsymbol{A}. \tag{21}$$

The convolution sum on the left-hand side is evaluated by using the 2/3 rule to avoid aliasing errors. In transform space it is then straightforward to obtain the Fourier expansion coefficients of $\boldsymbol{A}$. In addition, it is possible to obtain $\boldsymbol{G}_N$ via the Helmholtz decomposition (20). This procedure finally yields the following algorithm

$$\boldsymbol{G}_N(\boldsymbol{u}_N)\mathrm{e}^{h\delta t\nu\Delta} = \sum_{\boldsymbol{k}\in\mathbb{Z}^2} \frac{\mathrm{i}(k_y\boldsymbol{e}_x - k_x\boldsymbol{e}_y)}{k^2}[(\boldsymbol{u}_N\cdot\widetilde{\nabla})\omega_N]_{\boldsymbol{k}}\mathrm{e}^{-\nu k^2 h\delta t + \mathrm{i}\boldsymbol{k}\cdot\boldsymbol{x}}. \tag{22}$$

The penalization parameter ϵ can be chosen independent from the time step without additional FFT's (3 forward and 4 backward). Furthermore, it is not necessary to perform a Fourier expansion of the discontinuous restricted velocities Hu and Hv. Therefore, the only convergence limitations appear from the regularity of the penalized Navier–Stokes equations considered in Section 2.2.

3.3. Coherent vortex simulation

Coherent vortex simulation (CVS) introduced by Farge and co-workers [15,16] is a new method to compute turbulent flows. It is based on the wavelet filtered Navier–Stokes equations, whose solutions are computed in an adaptive wavelet basis. The wavelets are dynamically selected to track the flow evolution with a reduced number of modes (cf. [37,16,36,38]). The success of this methodology hinges on the ability of the wavelets to achieve a significant reduction in the number of modes needed to describe the flow evolution. In the following, we briefly summarize the adaptive wavelet method to solve the two-dimensional Navier–Stokes equations in velocity–vorticity formulation (5).

In the CVS computations, we employ a semi-implicit time scheme of second-order [17], i.e., an Euler–Backwards scheme for the diffusion term and an Adams–Bashforth scheme for the advection and penalization term. The explicit treatment of the advection and penalization terms implies a limitation of the time step size to guarantee stability, i.e. the time step has to satisfy the CFL condition and also has to be smaller than the penalization parameter. Discretizing (6) therewith we obtain

$$(\gamma - \nu\Delta)\omega^{n+1} = \frac{4}{3}\gamma\omega^{n} - \frac{1}{3}\gamma\omega^{n-1} + \mathcal{N}(2\omega^{n} - \omega^{n-1}) \tag{23}$$

$$\Delta\Psi^{n+1} = \omega^{n+1} \quad \text{and} \quad \mathbf{u}^{n+1} = \nabla^{\perp}\Psi^{n+1}, \tag{24}$$

where $\gamma = 2/(3\delta t)$, $\nabla^{\perp} = (-\partial_y, \partial_x)$ and Ψ denotes the stream function. Hence in each time step two elliptic problems have to be solved and a differential operator has to be applied. Formally, the above equations can be written in the abstract form $Lu = f$, where L is an elliptic operator with constant coefficients, corresponding to a Helmholtz type equation for ω with $L = (\gamma - \nu\Delta)$ and a Poisson equation for Ψ with $L = \Delta$.

For the spatial discretization we use a Petrov–Galerkin scheme. The trial functions are orthogonal wavelets and the test functions are operator-adapted wavelets. To solve the elliptic equations $Lu = f$ at time step t^{n+1} we develop u^{n+1} into an orthogonal wavelet series, *i.e.*, $u^{n+1} = \sum_{\lambda}\widetilde{u}_{\lambda}^{n+1}\psi_{\lambda}$, where $\lambda = (j, i_x, i_y, d)$ denotes the multi-index containing scale j, space i_x, i_y and direction information d. Requiring that the residuum vanishes with respect to all test functions $\theta_{\lambda'}$, we obtain a linear system for the unknown wavelet coefficients $\tilde{u}_{\lambda}^{n+1}$ of the solution u:

$$\sum_{\lambda}\tilde{u}_{\lambda}^{n+1}\langle L\psi_{\lambda}, \theta_{\lambda'}\rangle = \langle f, \theta_{\lambda'}\rangle. \tag{25}$$

The test functions θ are defined such that the stiffness matrix turns out to be the identity. Therefore the solution of $Lu = f$ reduces to a change of the basis, i.e., $u^{n+1} = \sum_{\lambda}\langle f, \theta_{\lambda}\rangle\psi_{\lambda}$.

The right-hand side f can then be developed into a biorthogonal operator adapted wavelet basis $f = \sum_{\lambda}\langle f, \theta_{\lambda}\rangle\mu_{\lambda}$, with $\theta_{\lambda} = L^{\star-1}\psi_{\lambda}$ and $\mu_{\lambda} = L\psi_{\lambda}$ (* denotes the adjoint operator). By construction θ and μ are biorthogonal, $\langle\theta_{\lambda}, \mu_{\lambda'}\rangle = \delta_{\lambda,\lambda'}$. It can be shown that both have similar localization properties in physical and Fourier space as has ψ and that they form a Riesz basis [17].

To get an adaptive space discretization for the problem $Lu = f$ we consider only the significant wavelet coefficients of the solution. Hence, we only retain coefficients $\tilde{u}_{\lambda}^{n}$ which have an absolute value larger than a given threshold $\tilde{\varepsilon}$, i.e., $|\tilde{u}_{\lambda}^{n}| > \tilde{\varepsilon}$. The corresponding coefficients are shown in Fig. 2 (white area under the solid line curve). The threshold $\tilde{\varepsilon}$ is not constant in time. It depends on the enstrophy Z (35) of the flow in the following way

$$\tilde{\varepsilon}(t) = \tilde{\varepsilon}_0\sqrt{Z(t)/Z(t_0)}. \tag{26}$$

with a constant $\tilde{\varepsilon}_0$. This choice is motivated for decaying flows to maintain the relative error in the enstrophy.

To be able to integrate the equation in time we have to account for the evolution of the solution in wavelet-coefficient space (indicated by the arrow in Fig. 2). Therefore, we add at time step t^n the local neighbors to the retained coefficients, which constitute a security zone (grey domain in Fig. 2). The equation is then solved in this enlarged coefficient set (white and grey region in Fig. 2) to obtain $\tilde{u}_{\lambda}^{n+1}$. Subsequently, we threshold the coefficients and retain only those with $|\tilde{u}_{\lambda}^{n+1}| > \tilde{\varepsilon}$ (coefficients under the dashed curve in Fig. 2). This strategy is applied in each time step and allows hence to track automatically the evolution of the solution in scale and space.

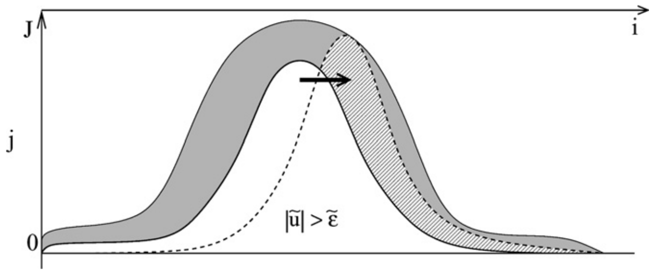

Fig. 2. Illustration of the dynamic adaption strategy in wavelet coefficient space. The vertical axis represents scale and the horizontal axis represents 1D space information denoted by j and i, respectively, in the multi-index λ. The white area under the solid curve represents the wavelet coefficients at t_n, the gray region is the security zone and the dashed region represents the distribution of the wavelet coefficients at the new time-level t_{n+1}.

The nonlinear term $f(u^n)$, where the wavelet coefficients of u^n are given is evaluated in physical space on a locally refined grid. This approach is similar to the pseudo-spectral evaluation of nonlinear terms used in spectral methods, and therefore this method is called pseudo-wavelet technique. The prerequisites, however, are that fast adaptive wavelet decomposition and reconstruction algorithms are available. This means that functions can be reconstructed on a locally refined grid from a sparse set of their significant wavelet coefficients and vice versa which are given in [17]. The method can be summarized as follows: starting from the significant wavelet coefficients of u, i.e., $|\tilde{u}_\lambda| > \tilde{\varepsilon}$, one reconstructs u on a locally refined grid, $u(x_\lambda)$. Then one can evaluate $f(u(x_\lambda))$ pointwise and the wavelet coefficients of f can be calculated using the adaptive decomposition to get $\widetilde{f}_\lambda$.

Finally, we have to calculate those scalar products of the r.h.s f with the test functions θ, to advance the solution in time. We compute $\tilde{u}_\lambda = \langle f, \theta_\lambda \rangle$ belonging to the enlarged coefficient set (white and gray region in Fig. 2). In summary the above algorithm is of $O(N^2)$ complexity, where N denotes the number of wavelet coefficients used in the computation per spatial direction.

3.4. Chebyshev spectral methods

Pseudospectral simulations were performed with numerical codes developed by Clercx [8] and Kramer [25] for the square bounded and a periodic channel geometry, respectively. For the square bounded domain the flow variables are expanded by Chebyshev polynomials in both directions. The solver of Kramer [25] is very similar to the solver of Clercx [8]. The main difference is that a Fourier expansion of the flow variables in the periodic direction has been applied. In the non-periodic direction the flow variables are represented by Chebyshev expansions as well. An advantage of the latter approach is that it is easier to achieve high-resolution computations both in the direction normal and tangential to the wall.

On the domain Ω_f, the vorticity problem can be written in the dimensionless form as put forward by Daube [12]

$$\begin{cases} \frac{\partial\omega}{\partial t} + (\mathbf{u}\cdot\nabla)\omega = \frac{1}{Re}\Delta\omega & \text{in } \Omega_\mathrm{f}\times[0,T] \\ \omega(\cdot,0) = \omega_0 & \text{in } \Omega_\mathrm{f} \\ \omega = (\nabla\times\mathbf{u})\cdot\boldsymbol{e}_z & \text{on } \partial\Omega_\mathrm{f}\times[0,T] \end{cases} \tag{27}$$

where ω_0 is the initial datum. The integral-scale Reynolds number is defined as $Re = UW/v$ (where U is a characteristic velocity of the flow, W the half width of the domain and v the kinematic viscosity of the fluid). The vorticity problem (27) has to be solved in combination with the Poisson problem

$$\begin{cases} \Delta\mathbf{u} = \boldsymbol{e}_z\times\nabla\omega & \text{in } \Omega_\mathrm{f}\times[0,T], \\ \mathbf{u} = 0 & \text{on } \partial\Omega_\mathrm{f}\times[0,T], \end{cases} \tag{28}$$

with $\mathbf{e}_z$ the unit vector perpendicular to the plane of the flow. Note that for the periodic channel geometry the no-slip boundary condition is only applied in the non-periodic direction. The time discretization in the square bounded geometry of the vorticity equation (27) consists of the second-order explicit Adams–Bashforth scheme for the advection term and the implicit Crank–Nicolson procedure for the diffusion term. For the periodic channel geometry a third-order backward difference scheme is applied for diffusion and extrapolation for the advection term.

4. Recovery of higher-order accuracy of Fourier schemes

Recall that the $C^1(\Omega)$ and $C^0(\Omega)$ continuity of respectively the velocity and pressure of the penalized Navier–Stokes equations are enforced by an asymptotically thin boundary layer. On the other hand, continuity of the higher derivatives is guaranteed in Ω_f and Ω_s (see Ref. [5]). Thus, in the limit $\epsilon\to 0$ the penalized solution converges to a piecewise continuous function. This might be a problem for Fourier spectral methods since the L_p convergence of both the continuous (9) and discrete Fourier expansions (16) depends on the global smoothness of a function. As a consequence the uniform convergence is exponential for analytic functions, but a localized discontinuity, on the other hand, makes the Fourier projection suffer from oscillatory behavior known as the Gibbs phenomenon. The uniform convergence is lost in the neighborhood of a discontinuity and the L_p convergence rate drops to first-order. Fortunately, the convergence rate for piecewise continuous functions in terms of moments against any analytic function $\phi(x)$ (or more rigorously stated in terms of Sobolev norm of negative order) is still excellent,

$$\left|\int_0^{2\pi}\{f_N(x)-f(x)\}\phi(x)\,\mathrm{d}x\right| \leqslant Kr^N \tag{29}$$

for some constant K and a constant r between zero and one. The only requirement is that f belongs to the space L_2 (see Ref. [4] for details). This demonstrates that nearby Gibbs oscillations cancel very rapidly in the weighted mean $\phi(x)$ being any smooth function.

Inspired by estimate (29) several techniques have been proposed to recover the pointwise convergence for the Fourier projections of piecewise continuous data. In this paper, we follow the so-called "mollification" approach introduced by Gottlieb and Tadmor [19] and later improved by Tadmor and Tanner [40]. It exploits the fast cancellation of the Gibbs oscillations and offers a robust, efficient and general purpose procedure for accurate reconstruction of piecewise continuous data, where tuning of the parameters and roundoff errors are completely avoided.

The basic idea is to equip the analytic weight function $\phi(x)$ in Eq. (29) with two parameters p and θ, such that it is charged to find a balance between localization of the function f and cancellation of neighboring Gibbs oscillations. To simplify notation we discuss the mollification process of the continuous Fourier expansion in 1D. It is however straightforward to apply the algorithm in 2D. The procedure can be expressed as a convolution integral of the form,

$$R[f_N](x) = \phi_{p,\theta}\times f_N(x) = \int_0^{2\pi} f_N(\bar{x})\phi_{p,\theta}(x-\bar{x})\,\mathrm{d}\bar{x}, \tag{30}$$

where the mollifier is defined as $\phi_{p,\theta}(z) = (1/\theta)\rho(z/\theta)D_p(z/\theta)$, with the Dirichlet kernel

$$D_p(\zeta) = \begin{cases} \frac{1}{2\pi}\frac{\sin((p+1/2)\zeta)}{\sin(\zeta/2)} & \text{if } \zeta \neq 0, 2\pi, \ldots \\ \frac{2p+1}{2\pi} & \text{if } \zeta = 0, 2\pi, \ldots \end{cases} \tag{31}$$

and a piecewise C^∞ weight function

$$\rho(\zeta) = \begin{cases} \mathrm{e}^{-10\zeta^2/(\pi^2-\zeta^2)} & \text{if } |\zeta| < \pi, \\ 0 & \text{if } |\zeta| \geqslant \pi. \end{cases} \tag{32}$$

The number of near-vanishing moments of the mollifier and thus the number of cancellations is controlled with p. The parameter θ handles the support $]-\theta\pi, \theta\pi[$ and should be as large as possible to allow a necessary amount of cancellation in the convolution integral (30). Due to the requirement of localized regularity of the function f it is not allowed to incorporate a discontinuity. For optimal convergence the support of the mollifier should be $\theta = \max(d(x)/\pi, 2\pi/N)$, where $d(x)$ represents the distance to the nearest jump discontinuity. Note that due to the symmetry of the mollifier it is not possible to use the mollification procedure on the discontinuity itself. An optimal choice for p depends in addition on the support of the mollifier, $p(x) = \kappa\theta(x)N/2$, where κ is an arbitrarily chosen parameter between 0 and 1. The same value $\kappa = 0.5$ is chosen as in the numerical validation of the method presented in Ref. [40]. In order to obtain finite-order convergence in a small region of $\mathcal{O}(1/N)$ around a discontinuity Tadmor and Tanner [40] have introduced normalization procedures that remove the higher-order moments of the mollifier. As a result, exponential convergence in the pointwise sense is recovered from the Fourier projection sufficiently far from a discontinuity. At a distance of $\mathcal{O}(1/N)$ fourth-order convergence is achieved and at least second-order convergence appears up to the discontinuity. In Ref. [40] an equivalent procedure is developed for the discrete Fourier expansion, with similar convergence results.

In this study, the mollification procedure is only applied as a postprocessing tool. A similar approach, although with a Gegenbauer postprocessing tool (see Ref. [20]), is successfully performed by Shu and Wong [39] on development of shocks in the solution of the Burgers equation and also in the 2D Euler equations by Don [14]. It should be emphasized that these are a posteriori results due to the lack of full theoretical justification. Gottlieb and Gottlieb [18] explain these results, however, by going back to the argument of Lax [28] on the suitability of Fourier spectral schemes on shock development in nonlinear hyperbolic systems. Nevertheless, it is not a priori known whether postprocessing can successfully recover the solution of the penalized Navier–Stokes equations as well.

5. Dipole–wall collision benchmark computation

The numerical simulations of Clercx and Bruneau [6] indicate that it is extremely difficult to obtain mode or grid-convergence for a dipole that collides with a no-slip boundary using a Chebyshev pseudospectral method or finite differences. Here, we focus on the convergence properties of a normal dipole–wall collision, i.e. the translation of the dipole being perpendicular to the wall, at an integral-scale Reynolds number $Re = \frac{UW}{\nu} = 1000$, based on the total kinetic energy of the flow (determining the average velocity U) and the half width W of the domain. Note that this value of Re is similar as in the 2D decaying turbulence simulations in square bounded domains by Clercx and Nielsen [9]. They used (initial) integral-scale Reynolds numbers varying between 5000 and 20,000, but the Reynolds number based on the vortex size in these runs was always in the range 700–2500. Therefore, the dipole–wall experiment at $Re = 1000$ can be seen as a novel test case to explore the possibility of pursuing DNS of wall bounded turbulence.

5.1. Setup and initial condition

The flow domain Ω_f is defined as

$$\Omega_\mathrm{f} = \{\boldsymbol{x} \in \mathbb{R}^2 | -1 \leqslant x \leqslant 1, -1 \leqslant y \leqslant 1\}.$$

The initial (scalar) vorticity field ω_0 and velocity field $\mathbf{u}_0$ should vanish at the boundary, which guarantees absence of artificial boundary layers due to enforcing the no-slip condition at $t = 0$. In order to satisfy these constraints, two equally strong, oppositely signed, isolated monopoles are put close to each other near the center of the container. The vorticity distribution of the isolated monopoles is chosen as

$$\omega_0 = \omega_\mathrm{e}(1 - (r/r_0)^2)\exp(-(r/r_0)^2), \tag{33}$$

with $r = (x^2 + y^2)^{1/2}$ the distance from the center of the monopole, r_0 its dimensionless 'radius' (at which the vorticity changes sign) and ω_e its dimensionless extremum vorticity value (in $r = 0$). In the present simulations, the exact numerical value for the radius of the monopoles is $r_0 = 0.1$, and $\omega_\mathrm{e} = 299.528385375226$. With this value of r_0 the vorticity at the boundary (at $r \approx 1$) is virtually zero, as can be concluded by substituting the numerical value of the ratio r/r_0 in Eq. (33).

This value of ω_e is determined by the condition that the total kinetic energy of the dipolar flow field

$$E(t) = \frac{1}{2}\int_{-1}^{1}\int_{-1}^{1}\mathbf{u}^2(\mathbf{x},t)\mathrm{d}x\,\mathrm{d}y, \tag{34}$$

is normalized to $E(0) = 2$ for all runs. As a consequence, both U and the halfwidth of the domain W are fixed and the Reynolds number is defined as $Re = UW/\nu$. The total enstrophy of the dipolar flow field is defined by

$$Z(t) = \frac{1}{2}\int_{-1}^{1}\int_{-1}^{1}\omega^2(\mathbf{x},t)\mathrm{d}x\,\mathrm{d}y, \tag{35}$$

with $Z(0) \approx 800$. The exact numerical values for the initial position of the two isolated monopoles is $\{(x_1, y_1), (x_2, y_2)\} = \{(0, 0.1), (0, -0.1)\}$. The initial datum $\mathbf{u}_0 = (u_0, v_0)$ for the integration of the Navier–Stokes equations in primitive variables can be derived straightforwardly for a couple of isolated monopoles, satisfying Eq. (33) and is then given by:

$$\begin{aligned} u_0 &= -\frac{1}{2}|\omega_\mathrm{e}|(y - y_1)\exp(-(r_1/r_0)^2) + \frac{1}{2}|\omega_\mathrm{e}|(y - y_2)\exp(-(r_2/r_0)^2) \\ v_0 &= \frac{1}{2}|\omega_\mathrm{e}|(x - x_1)\exp(-(r_1/r_0)^2) - \frac{1}{2}|\omega_\mathrm{e}|(x - x_2)\exp(-(r_2/r_0)^2), \end{aligned} \tag{36}$$

with $r_1^2 = (x - x_1)^2 + (y - y_1)^2$ and $r_2^2 = (x - x_2)^2 + (y - y_2)^2$. This initial datum also proves that the no-slip condition is sufficiently well guaranteed by our choice $r_0 = 0.1$ (note that $\mathrm{e}^{-(r/r_0)^2} \approx \mathrm{e}^{-100} \approx 10^{-44}$).

5.2. Chebyshev–Fourier and Chebyshev benchmark computations

Fig. 3 gives an overview of the normal dipole–wall collision obtained by a Chebyshev–Fourier benchmark computation, using 1024 Chebyshev modes and 2048 active Fourier modes with a time step $\delta t = 10^{-5}$. As the dipole impinges the wall at $t \approx 0.3$ relatively thin boundary layers are formed containing oppositely-signed vorticity compared to the approaching (primary) monopoles. In addition high-amplitude vorticity filaments are stripped from the boundary layers yielding two new (secondary) vortex cores, as can be seen in the vorticity contour plot at $t = 0.4$. The trajectories of the new vortices are strongly curved resulting in a second collision at $t \approx 0.6$. For $t \gtrsim 0.8$ there is no appreciable production of vorticity at the no-slip wall anymore while the vorticity already present is slowly dissipated. It is found by Clercx and Bruneau [6] that an extremely fine discretization is required for accurate quantitative results. Especially for simulations with long integration times compared with the time t_1 of the primary collision. In particular underresolved high-amplitude vorticity patches near the no-slip wall (visible in Fig. 3) can possibly deteriorate the accuracy in course of time.

To analyze the quality of the Chebyshev and Chebyshev–Fourier computations we analyze the relative error in the vorticity

$$\delta_N = \frac{\|\omega(N) - \omega(N_{\max})\|_{L^2}}{\|\omega(N_{\max})\|_{L^\infty}}, \tag{37}$$

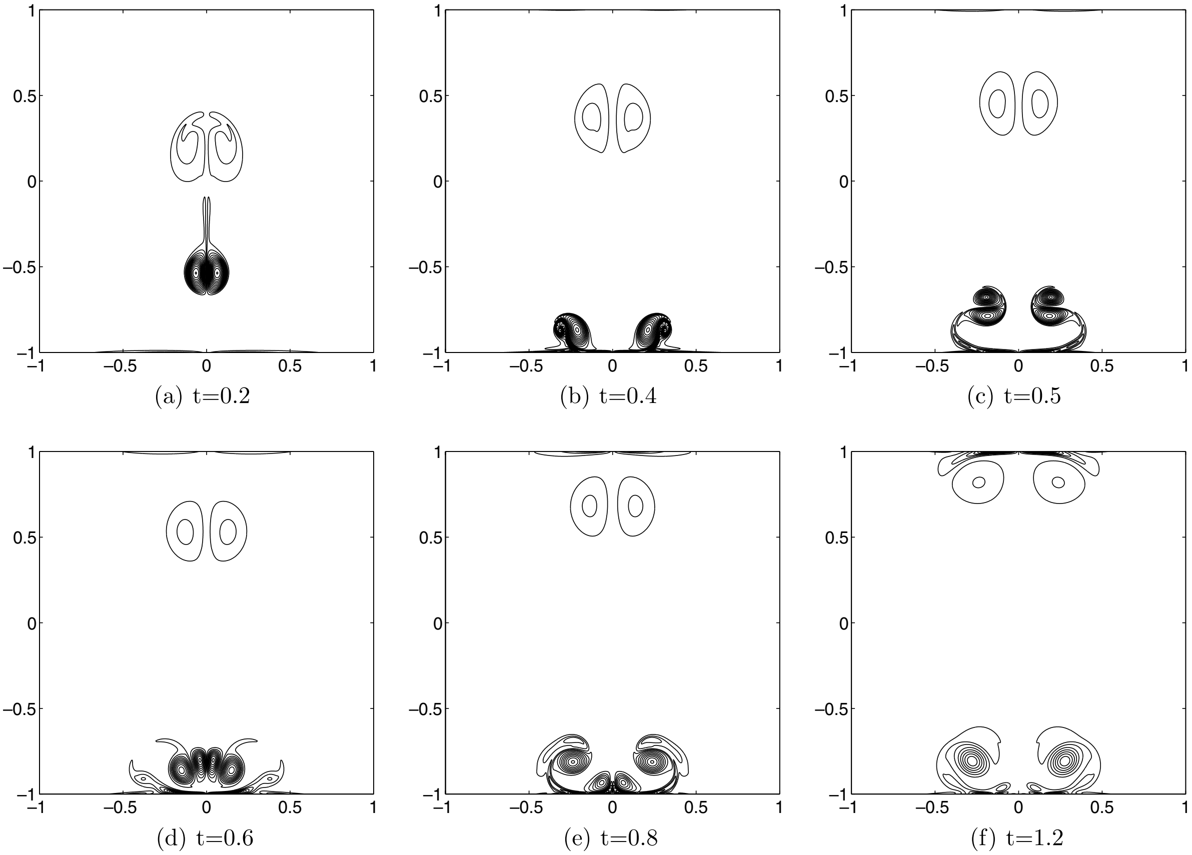

(a) t=0.2 (b) t=0.4 (c) t=0.5

(d) t=0.6 (e) t=0.8 (f) t=1.2

Fig. 3. Contour plots of the vorticity field of a normal dipole–wall collision with $Re = 1000$. In this simulation 1024 Chebyshev modes are used perpendicular to the wall and 2048 Fourier modes for the periodic channel direction. The time step is given by $\delta t = 10^{-5}$. Contour levels are drawn for −270, ..., −50, −30, −10, 10, 30, 50, ..., 270.

where $\omega(N)$ is the approximation of the vorticity with resolution N and $N_{\max}$ is the maximum N that is available. The highest-resolution computations that are performed for the square bounded domain have 640 Chebyshev modes in both directions. For the periodic channel domain a maximum of 1024 Chebyshev modes for the non-periodic direction and 2048 active Fourier modes is used for the periodic direction. To estimate the error of the computations lower resolution computations are performed as well. For the square bounded case a second computation is conducted with 512 Chebyshev modes in both directions and the periodic channel with 512 Chebyshev modes versus 1024 active Fourier modes. The time step is fixed for all computations, i.e., $\delta t = 10^{-5}$. It is found that the truncation error δ_N is less than 1.2×10^{-4} for the square bounded case. Clercx and Bruneau [6] have shown that the truncation error of the Chebyshev scheme decays exponentially with N. They considered the dipole–wall experiment for $Re = 1250$ and $N_{\max} = 512$ in both directions. The order of magnitude of the truncation error observed here for $Re = 1000$ and $N_{\max} = 640$ is consistent with the results of Clercx and Bruneau [6]. The error δ_N for the periodic channel geometry is less than 8.2×10^{-5} for $t \leqslant 2.0$. Therefore, the high-resolution computations in both geometries can be considered as sufficiently accurate benchmark computations.

6. Convergence analysis of Fourier schemes

To simulate the dipole–wall collision with volume-penalization the flow domain Ω_f defined in Section 5.1 is embedded in the channel geometry of Fig. 1b. The computational domain Ω is defined as

$$\Omega = \{\boldsymbol{x} \in \mathbb{R}^2 | -1 \leqslant x \leqslant 1, -(1+\delta_w) \leqslant y \leqslant (1+\delta_w)\}, \tag{38}$$

where the wall thickness δ_w is chosen such that there is a set of grid points on the interface between the fluid and the solid (porous) material. It is found that decreasing δ_w from 10% down to 1% of the channel width does not change the computational result significantly. To reduce the number of grid points inside Ω_s as much as possible the wall thickness δ_w is fixed to about 1% of the domain size for the Fourier spectral simulations presented here.

Due to the continuity restrictions of the solution of the penalized Navier–Stokes equations (see Section 3) on $\partial\Omega_f$ it can be expected that the Fourier projections of the different flow variables will suffer from the Gibbs phenomenon. The key question is, however, whether the low convergence rate of the Fourier projection will in addition prevent proper convergence of the Fourier spectral scheme or that higher-order accuracy can be recovered by the mollification technique proposed by Tadmor and Tanner [40] (or alternative techniques such as high-wavenumber filtering [29] and Gegenbauer postprocessing [21]).

6.1. Gibbs oscillations

Fig. 4. presents the isolines of the vorticity obtained by the Fourier spectral solver with 1364 active Fourier modes in both directions using $\epsilon = 2.5 \times 10^{-5}$ and implicit treatment of the Darcy drag with a time step of $\delta t = 10^{-5}$. As the dipole impinges the wall strong oscillations in the vorticity isolines become indeed apparent, as is evident from Fig. 4. Note that only one-half of the domain is shown because of the symmetry of a normal dipole–wall collision. The oscillations are more pronounced near the wall than in the interior of the flow domain. An important observation is that the wiggles automatically disappear as the vortex moves into the interior of the flow domain, $t = 0.5$ in Fig. 4d. In addition Fig. 5 shows the mollified results obtained by the recovery method of Tadmor and Tanner [40] applied to the computational output presented in Fig. 4. It reveals strong correspondence with the Chebyshev–Fourier benchmark computations. This indicates that the observed oscillations do not have a serious dynamical effect on the evolution of the dipole–wall collision.

6.2. Truncation error

In order to investigate the scaling behavior of the truncation error the simulations are compared with the highest available resolution of 2730×2730 active number of Fourier modes (computed with 4096×4096 Fourier modes to prevent aliasing errors), while the penalization parameter is fixed for all computations at a value of $\epsilon = 2.5 \times 10^{-5}$. This value is chosen such that it is feasible to test both the implicit and explicit

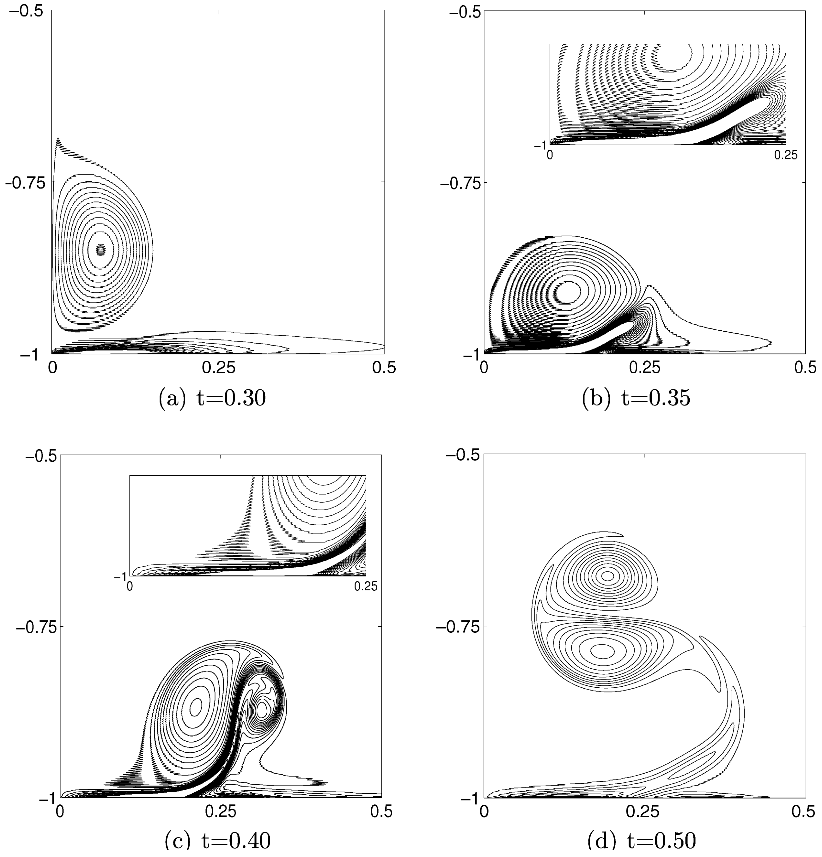

(a) t=0.30 (b) t=0.35

(c) t=0.40 (d) t=0.50

Fig. 4. Contour plots of the vorticity field of a normal dipole–wall collision with $Re = 1000$ using 1364×1364 active Fourier modes, $\delta t = 10^{-5}$ and $\epsilon = 2.5 \times 10^{-5}$ with an implicit scheme. Contour levels are drawn for −270, …, −50, −30, −10, 10, 30, 50, …, 270.

implementation of the Darcy drag efficiently. Note that for the explicit implementation the time step has to be in the same order as the penalization parameter. As a consequence, a smaller value for ϵ would result in a blow up of the amount of wall-clock time. On the other hand, $\epsilon = 2.5 \times 10^{-5}$ is small enough to have an acceptable correspondence with the Chebyshev–Fourier benchmark computation, which satisfy the no-slip condition within machine-precision accuracy.

The mollification procedure of Tadmor and Tanner [40] involves a symmetric mollifier that gives second-order accuracy in the immediate vicinity of a discontinuity (the wall in this case) and higher-order accuracy when moving away from the discontinuity. Therefore, we decompose the domain in an interior part Ω_{int} ranging from $x = [-1, 1]$ and $y = [-0.99, 0.99]$ and a boundary zone. Only in the interior part high-order recovery of the Fourier projection can be expected for all the resolutions considered here. Fig. 6 demonstrates the convergence behavior in the boundary zone. A cross-section of the viscous boundary is presented at the point where the vorticity on the wall has a maximum. Fig. 6a shows that the amplitude of the oscillations in the Fourier projection decreases slowly by increasing the resolution. The vorticity value on the wall reflects a well-known convergence property of Fourier series

$$\lim_{N\to\infty} \omega_N(x) = \frac{\omega(x_-) + \omega(x_+)}{2}, \tag{39}$$

where x_- and x_+ denote the limits from below and above x, respectively. Since the vorticity inside the obstacle is negligible (see Section 2.2) the projection ω_N underpredicts the vorticity on the wall by a factor two. Recall that C^0 continuity of the vorticity is enforced by an asymptotically thin boundary layer inside the obstacle proportional to $\sqrt{\nu\epsilon}$. The resolution of the computations is, however, too low to resolve this boundary layer.

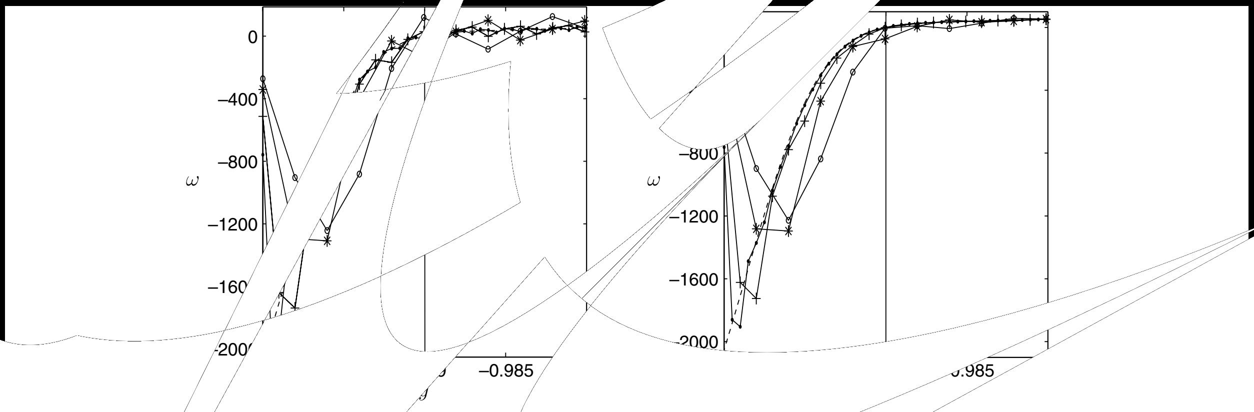

ier projectio , After rec

ctio along the line $x =$, Chebyshev–Fo
δt 10^{-5}, with different number of active Fourier mode
ose

The ecovered F converges smoothly towards the benchmark computation. Note at this ref of the computation, as well as, the accuracy of the postprocessing impr ve with N

he conv is analyzed by considering the error

$$\delta_{} \frac{(\Omega_{\text{int}})}{\|_{L^\infty(\Omega_{\text{f}})}},$$

where N represents the simulations conducted with less than 2730 active Fourier modes in both directions. The time step is fixed for all computations, *i.e.*, $\delta t = 10^{-5}$ consistent with the CFL condition of the high-resolution computation with 2730×2730 active Fourier modes. The convergence rate of the Fourier projection presented in Fig. 7 depends on the time considered. During the collision process, in particular at $t = 0.3$, $t = 0.35$ and $t = 0.4$, the error of the Fourier projection only shows first order decay, while at some later time, for example, $t = 0.5$ the error decays faster. The error of the mollified vorticity fields shows, however, fast decay at least proportional to $N^{-2.5}$ for all times. From these observations it is difficult to determine the exact value for the order of the scheme. Especially, because it is not sure how the mollified error is behaving with either a specific power law or exponentially. Note that the slope increases when moving towards the higher end of the spectral range considered here. This might indicate that the error of the postprocessed results behaves exponential or that higher-order convergence appears after reaching a specific resolution related to the thickness of the viscous boundary layer. At $t = 0.5$ the mollification procedure does not improve the scaling of the truncation error, which can be related to absence of strong oscillations in the vorticity isolines in Fig. 4d. The

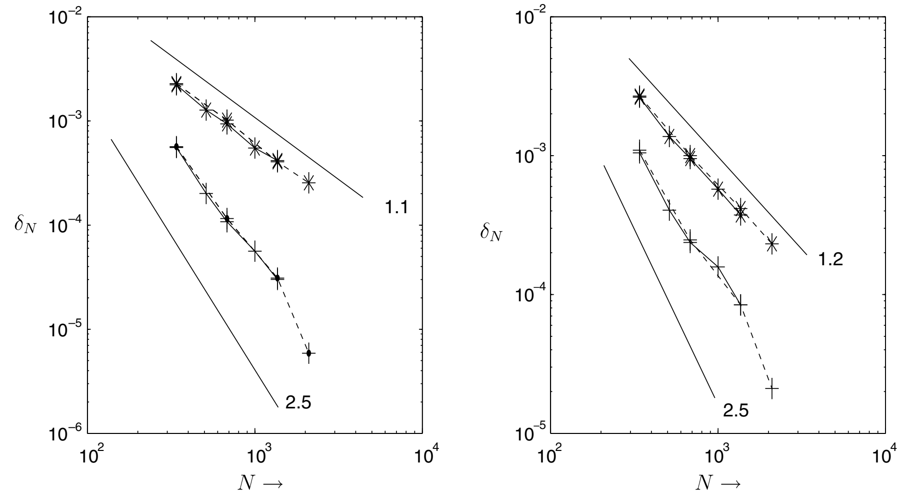

(a) $t = 0.3$ (b) $t = 0.35$

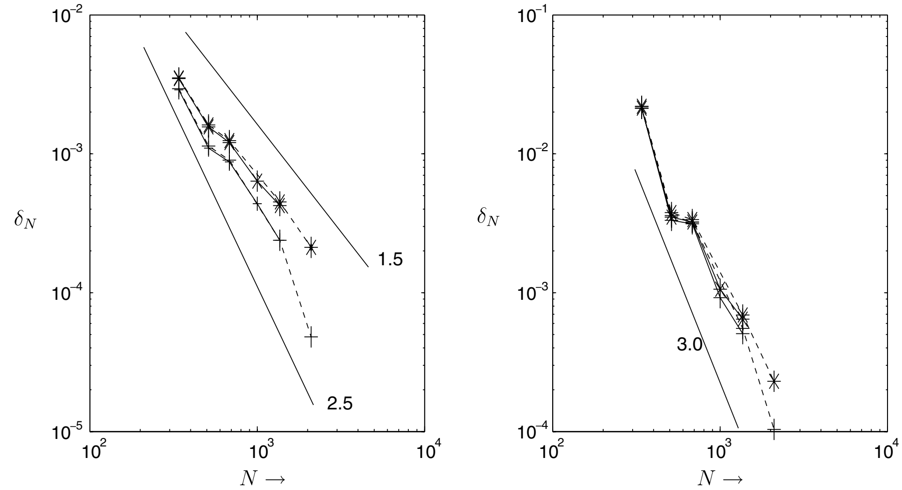

(c) $t = 0.4$ (d) $t = 0.5$

Fig. 7. Truncation error δ_N versus number of active Fourier modes N. Explicit (solid) and implicit (dashed) implementation of Darcy drag. The error of the Fourier projection (stars) and the mollified result (plus signs).

schemes of Sections 3.1 and 3.2 with an explicit and implicit treatment of the Darcy drag respectively, show a similar decay of the truncation error as can be deduced from Fig. 7.

6.3. Long-time integrations and global quantities

Some additional convergence results are presented in Fig. 8, concerning the total kinetic energy and total enstrophy of the flow. The computation with penalization parameter $\epsilon = 10^{-3}$ and $N = 682$ active Fourier modes shows a stronger decay of the total kinetic energy, while the total enstrophy is strongly underestimated. Setting $\epsilon = 10^{-8}$ and $N = 2730$ yields a curve $E(t)$ that is on top of the benchmark computation. The curve $Z(t)$ of the total enstrophy coincides with the benchmark almost everywhere but slightly underpredicts the maximum value of the enstrophy at $t = 0.35$. About 90% of the enstrophy is contained in the boundary layer presented in Fig. 6, especially the values on the wall itself strongly contribute to the total enstrophy. Unfortunately, we are not able to reconstruct the vorticity in the immediate vicinity of the wall and on the wall itself (see Fig. 6). This explains why the maximum enstrophy is slightly underestimated (a deviation of approximately 1%). If, however, the vorticity value on the wall is corrected with a factor two related to the convergence property (39) the error becomes less than 3.0×10^{-3}.

As reported by Clercx and Bruneau [6] especially long-time integrations beyond the first dipole–wall collision are difficult to resolve properly. In Fig. 9, the vorticity isolines are shown for a long-time integration using $N = 1364$ active Fourier modes, a penalization parameter $\epsilon = 10^{-8}$ and a time step $\delta t = 10^{-5}$. It clearly shows that convergence can be achieved as well for long-time integrations by setting the resolution and penalization parameter appropriately. Furthermore, the larger time integrations support the observation that Gibbs oscillations do not trigger any significant dynamical effects.

7. Convergence analysis of coherent vortex simulation (CVS)

In the following, we present results of coherent vortex simulations using the adaptive wavelet method ([35–38]) presented in subsection 3.3. The CVS simulations are conducted in the square bounded geometry, see Fig. 1c, the wall thickness $\delta_w = 0.1$ for all four side walls (note that $\Omega_f = [-1,1] \times [-1,1]$). First, we inspect the vorticity isolines computed with CVS versus a high-resolution Chebyshev computation. Then, we consider the compression rate of the degrees of freedom by the coherent vortex simulation method. In addition, we analyze the scaling behavior of the discretization error using different resolutions (128^2, 256^2, 512^2 and 1024^2) for

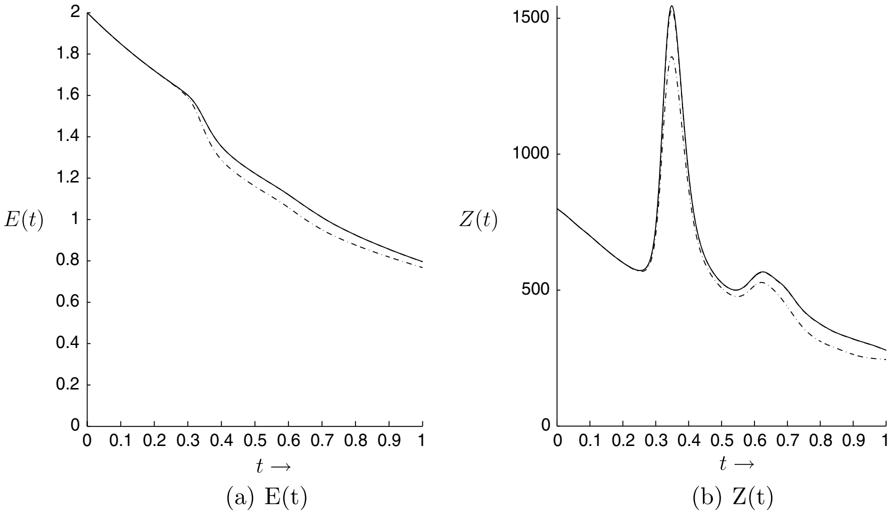

(a) E(t) (b) Z(t)

Fig. 8. Total kinetic energy $E(t)$ and enstrophy $Z(t)$ of a computation with setting $\epsilon = 10^{-3}$, $N = 682$, $\delta t = 10^{-5}$ (dashed-dot) and $\epsilon = 10^{-8}$, $N = 2730$, $\delta t = 10^{-5}$ compared with Chebyshev–Fourier benchmark computation (solid).

the CVS computations. Finally, it is checked if it is possible to further reduce the number of wavelet coefficients by varying the threshold $\tilde{\varepsilon}_0$ while keeping the number of grid points fixed.

7.1. Visualization

Fig. 10 visualizes the isolines of vorticity at $t = 0.4$ for a CVS computation using 1024^2 gridpoints and a time step $\delta t = 5 \times 10^{-5}$ compared to a Chebyshev benchmark result with 640 Chebyshev modes in both directions using a time step $\delta t = 1.25 \times 10^{-5}$. Although both simulations yield isolines which are very close to each other, one also observes that the symmetry around the y-axis is slightly broken in the CVS computation. A magnification of the left dipole half yields almost coinciding isolines, while a magnification of the other half in Fig. 10b visualizes some small deviations of the isolines compared to the Chebyshev benchmark computation. This is due to the wavelet discretization which is symmetric on a regular grid, however, the applied thresholding introduces some slight asymmetry on the locally refined grid which is not perfectly symmetric neither (cf. Fig. 11). Focussing on the vorticity isolines of the secondary vortex pair moving to the top of the domain we see in Fig. 10a that they differ slightly from the benchmark computation. This can be explained by the fil-

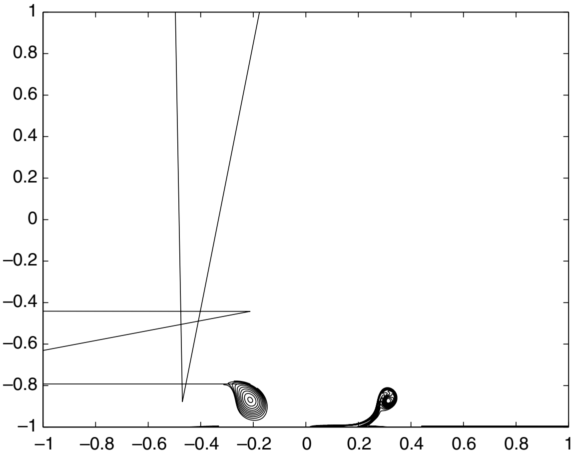

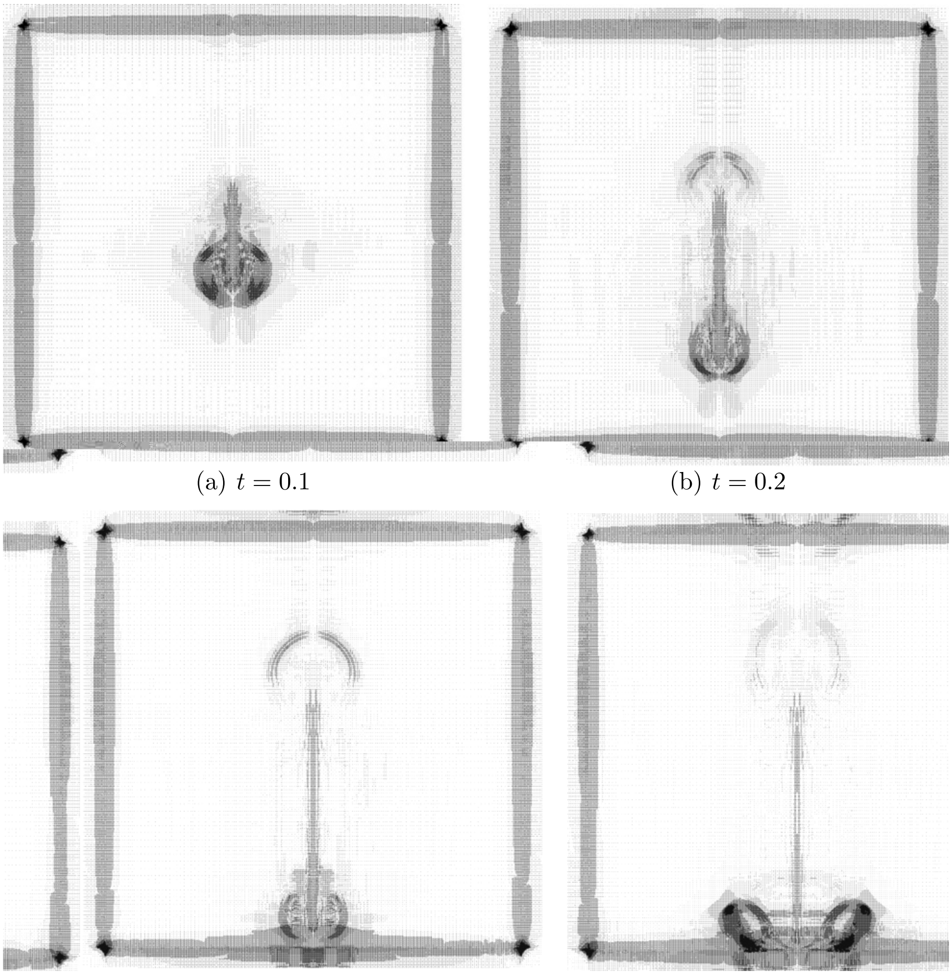

(a) $t = 0.1$ (b) $t = 0.2$

(c) $t = 0.3$ (d) $t = 0.4$

Fig. 11. Adaptive grid at $t = 0.1$, 0.2, 0.3 and 0.4 for CVS computation with 1024 grid points in both directions. The number of wavelets are 93,674, 104,711, 112,065 and 124,364 for $t = 0.1$, 0.2, 0.3 and 0.4, respectively.

tering effect of CVS. In each time step weak wavelet coefficients are filtered out, which correspond to weak vorticity contributions. As the secondary vortex pair contains much less enstrophy than the primary one it is more affected by the CVS filtering. We find that the CVS-1024 result exhibits no Gibbs oscillations like the Fourier computations. Therefore we decided not to apply any postprocessing to the CVS results.

7.2. Grid adaptation

To illustrate the dynamical adaption strategy of the CVS computations we plot in Fig. 11 the locally refined grids at different instants, $t = 0.1$, 0.2, 0.3 and 0.4. The computation has been performed with a maximum of $J = 10$ available scales, corresponding to a maximum number of 1024^2 unknowns, a fixed time step of $\delta t = 5 \times 10^{-5}$ and a threshold value of $\tilde{\varepsilon}_0 = 10^{-5}$. The penalization parameter was chosen as $\epsilon = 10^{-4}$. Note that without penalization the time step is only limited by the CFL-condition, which would allow a larger time step of $\delta t = 5 \times 10^{-4}$ for the CVS computations up to 1024^2 grid points. However, the explicit treatment of Darcy drag constitutes a restriction on the time step required for stable second-order time integration. In Fig. 11, we observe that the grid automatically tracks the time evolution of the dipole. In regions of strong gradients we find fine grid spacing while in quiescent regions the grid is coarsened. At the boundary of the domain, i.e. at the interface between the penalized region and the fluid domain, the grid is also refined to be able to resolve the strong gradients of vorticity. The finest scale $J = 10$ present in the CVS-1024 computation corresponds to the total number of wavelet modes N of $2^{2J} = 1024^2 = 1{,}048{,}576$. The time evolution of the number of active wavelet modes N_{w} for the CVS-1024 run, with and without the security zone (cf. Subsection 3.3), is depicted in Fig. 12. Both numbers are increasing also after the first collision. This can be explained by the choice (26) for the threshold $\tilde{\varepsilon}$. The threshold decreases with the total enstrophy retaining more modes in the computation. At $t = 0.1$, 0.2, 0.3 and 0.4 the computation (without security zone) uses 93,674, 104,711, 112,065 and 124,364 wavelet modes, respectively, i.e. less than 12% of the total number of modes.

A comparison of the total kinetic energy and enstrophy evolution of the CVS-1024 run with the Chebyshev benchmark with 640 Chebyshev modes in both directions is given in Fig. 13. It shows that the CVS computation closely follows the reference Chebyshev computation. Both total kinetic energy and enstrophy of the CVS computation are slightly below the reference run. To quantify the errors between the two methods we compute the relative maximum error for the energy, $\max|(E(t) - E^{\mathrm{cvs}}(t))/(E(t))|$, and for the enstrophy $\max|(Z(t) - Z^{\mathrm{cvs}}(t))/Z(t)|$. For the former we find a value below 0.8% while the latter is below 2.8%. Note that the computed error is the sum of the discretization and penalization error (Gibbs oscillations are not present in the CVS runs).

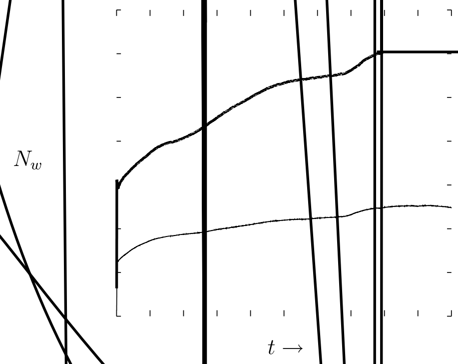

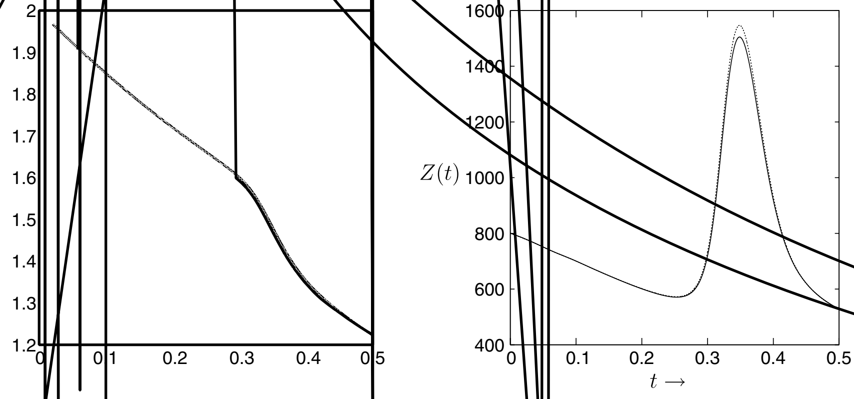

(a) Energy (b) Enstrophy

Fig. 13. Comparison of $E(t)$ (a) and $Z(t)$ (b) between the CVS run on 1024^2-grid, $\delta t = 5 \times 10^{-5}$, and penalization parameter $\epsilon = 10^{-4}$ (solid) and the Chebyshev run with 640^2 modes (dots) and $\delta t = 1.25 \times 10^{-5}$.

The time evolution of the wavelet modes for CVS computations with $N = 256^2$, $N = 512^2$ and $N = 1024^2$ grid points with a fixed time step $\delta t = 5 \times 10^{-5}$ is shown in Fig. 14. The compression rate improves with increasing resolution. For 256^2 almost all the coefficients (including security zone) are used at $t = 0.5$ (about 90%), while for 1024^2 less than 30% are used.

7.3. Error analysis

To quantify the error of the CVS computations we plot in Fig. 15a the normalized error in the vorticity of (i) the CVS computations with respect to the Chebyshev-640 reference computation and (ii) with respect to the CVS computation on the finest grid with 1024^2 grid points, note the double logarithmic presentation. Both curves show a power law behavior with a slope of 1.47. In Fig. 15b, a cross-section of the viscous boundary layer is shown at $t = 0.35$ along a line $x = 0.083$. From this figure it can be deduced that the

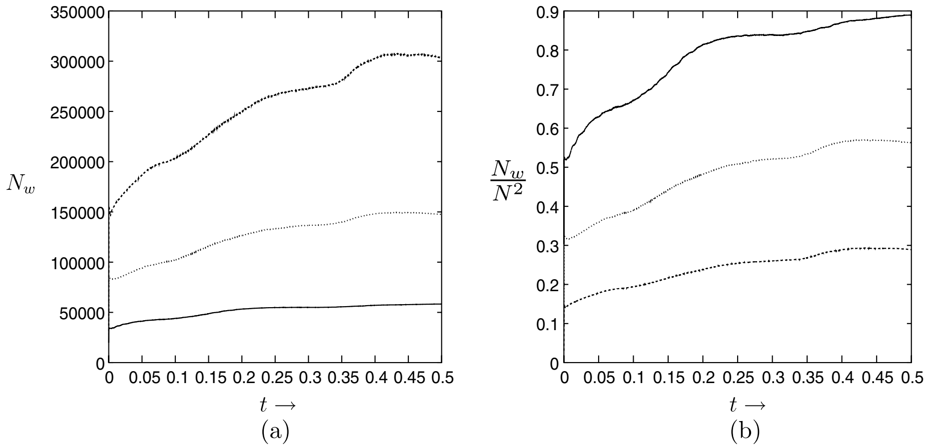

Fig. 14. Time evolution of the (a) number of wavelet coefficients N_w with security zone and (b) number of wavelet coefficients normalized with total number of grid points N for the CVS 256^2 grid points (solid) and $\delta t = 10^{-4}$, 512^2 grid points and $\delta t = 10^{-4}$(dots) and 1024^2 grid with $\delta t = 5 \times 10^{-5}$ (dashed) runs.

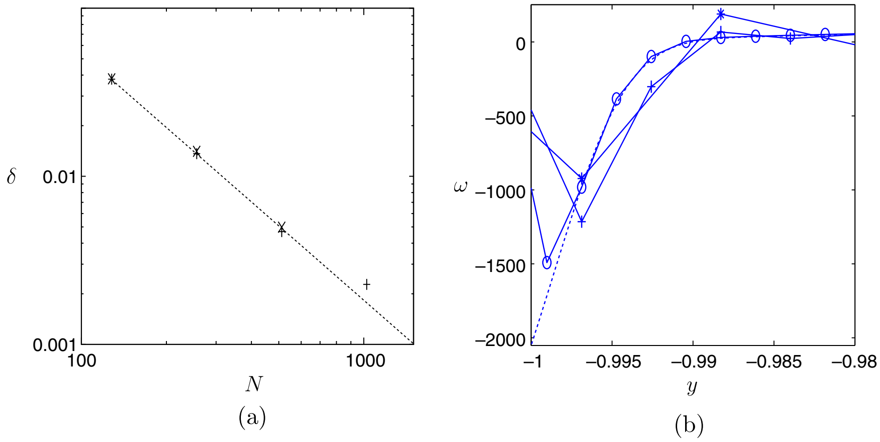

Fig. 15. Panel (a) shows the normalized L_2-error in the vorticity δ versus Chebyshev benchmark with 640^2 modes and $\delta t = 1.25 \times 10^{-5}$ (+) and the error with respect to the CVS computation on 1024^2 grid with time-step $\delta t = 5 \times 10^{-5}$ and $\epsilon = 10^{-4}$ (x) and the power law $47.05N^{-1.47}$ (dashed) obtained fitting the (+). Panel (b) shows the cross section of the vorticity similar along the line $x = 0.083$ at $t = 0.35$ (see Fig. 6) using different grids 256^2 (stars), 512^2 (plus signs) and 1024^2 (open circles) and benchmark computation using 640 Chebyshev modes in both directions and $\delta t = 1.25 \times 10^{-5}$ (dashed).

CVS result with 1024^2-grid is capable to capture the vorticity profile of the viscous boundary layer reasonably well. The behavior on the wall itself is not a result of Gibbs effect. It is a result of the implementation of the mask function in the CVS computations, which does not guarantee that there is a set of grid points on the wall at $y = -1$. The vorticity at the grid points inside the obstacle $y < -1$ is approximately zero. Recall that the solution of the penalized Navier–Stokes equation inside the obstacle can be described by Darcy flow, which has no rotation. As a consequence, there is no vorticity inside the obstacle. Interpolation between the grid point inside the obstacle and in the flow gives a wiggle near the wall at $y = -1$ in Fig. 15b. From the fit in Fig. 15a, we could deduce that the CVS method is of order 1.5 (in terms of vorticity), which is similar to the order of the Fourier spectral schemes without postprocessing. However, we should be careful with this conclusion, because the measurements are obtained in the regime where the number of grid points inside the viscous boundary layer is less than four. Here, the boundary-layer thickness δ based on the ratio of vorticity and vorticity gradients on the wall is defined as $\delta \approx \frac{1}{4\sqrt{Re}}$, see Ref. [6]. Hence, it cannot be ruled out that finer grid computations would yield different scaling behavior of the error, especially beyond a critical grid size that is proportional to the boundary-layer thickness. Unfortunately, higher-resolution computations are not yet feasible, because the current code does not run in parallel. On the other hand, Clercx and Bruneau [6] found that about five grid points inside the boundary layer are necessary to achieve grid-convergence for the normal dipole–wall collision experiment with a second-order (in velocity) finite-difference scheme. Considering the decay rate of the error in the vorticity, we expect that grid-convergence is achieved for the CVS-1024 computation.

7.4. Influence of the penalization parameter and reduction of wavelet coefficients

Different CVS computations have been performed to check the influence of the penalization parameter ϵ and of the threshold $\tilde{\epsilon}_0$ of the wavelet coefficients. In Fig. 16a, we plot the time evolution of the enstrophy for CVS-512 using three different values of the penalization parameter ϵ. The amount of enstrophy production on the wall increases significantly with the penalization parameter in the range $\epsilon = 10^{-2}$ to $\epsilon = 10^{-4}$. For the penalization parameter $\epsilon = 10^{-2}$, the accuracy becomes extremely poor, as can be seen in Fig. 16a. A second set of simulations is conducted to analyze the effect of $\tilde{\epsilon}_0$ on the enstrophy production. It is found that in the range $\tilde{\epsilon}_0 = 10^{-4}$ to $\tilde{\epsilon}_0 = 10^{-6}$ the maximal difference in $Z(t)$ lays within machine precision. However, the number of wavelet coefficients used in the $\tilde{\epsilon}_0 = 10^{-4}$ run is two times smaller than in the $\tilde{\epsilon}_0 = 10^{-6}$ computation, which can be deduced from Fig. 16b. As the computing time is linear with the number of wavelet modes used, for the same accuracy, a speed-up by a factor two can be obtained.

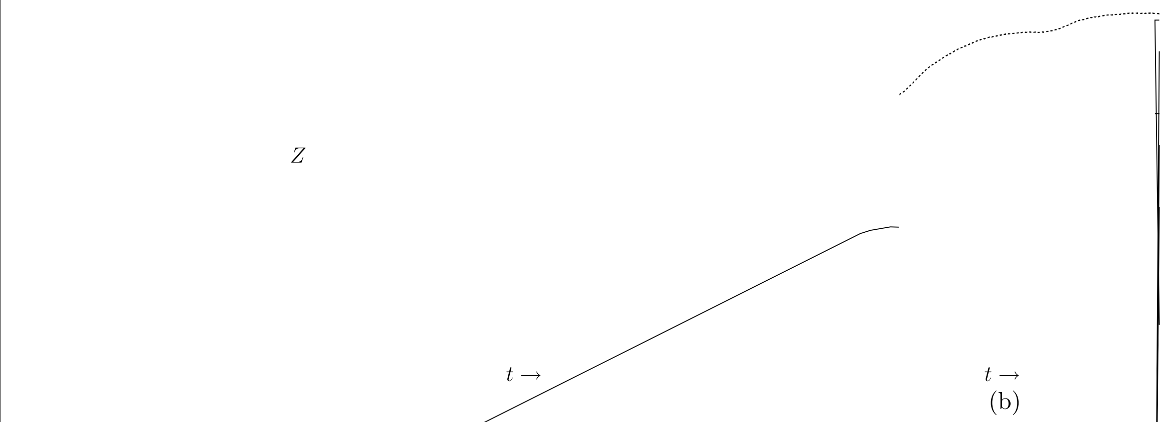

(b)

Fig. 16. Enstrophy versus time for three different values of the penalization parameter $\epsilon = 10^{-2}$ (dashed), $\epsilon = 10^{-3}$ (dots) and $\epsilon = 10^{-4}$ (solid), threshold $\tilde{\epsilon}_0 = 10^{-5}$ is fixed (a). Number of wavelet coefficients N_w with security zone for three different values of the threshold $\tilde{\epsilon}_0 = 10^{-4}$, $\tilde{\epsilon}_0 = 10^{-5}$ and $\tilde{\epsilon}_0 = 10^{-6}$ with penalization parameter $\epsilon = 10^{-4}$ fixed (b).

8. Penalization error

In this section, we focus on the penalization error δ_ϵ corresponding to the differences between the solution of the Navier–Stokes equations with no-slip boundary condition and the solution of the penalized Navier–Stokes equations. The challenge is to find a balance between the truncation and the penalization error by an optimal choice for ϵ for every N. Fig. 17 shows the vorticity isolines of runs where both the penalization parameter ranges from $\epsilon = 10^{-3}$ to $\epsilon = 10^{-8}$ and the number of active Fourier modes from $N = 682$ to $N = 2730$. The combination of penalization parameter and number of active Fourier modes is chosen such that an optimal setting is achieved, i.e., increasing N does not improve the accuracy significantly. The largest value of the penalization parameter, $\epsilon = 10^{-3}$, yields a slightly different vortex path compared with the benchmark computation. Especially, after the second collision at $t = 0.8$ it is seen that the secondary vortex core is not strong enough to bend the vortex system sufficiently outward (see Fig. 17a). This might be related to the amount of vorticity that is produced on the wall and in addition advected into the interior. As the penalization parameter is decreased, more vorticity is produced on the wall such that the resulting secondary vortex becomes stronger, finally resulting in acceptable converged vorticity isolines.

Fig. 18a shows the total error δ_{tot}, that is the sum of the truncation error δ_N and the penalization error δ_ϵ. It is calculated by using the high-resolution Chebyshev–Fourier benchmark computation with 1024 Chebyshev modes in the wall direction and 2048 Fourier modes in the periodic channel direction. As can be deduced from Fig. 18a it is possible to improve the decay rate of the total error versus N by taking sufficiently small values for the penalization parameter. For every ϵ a saturation level emerges at a specific N, e.g. for $\epsilon = 10^{-4}$ at $N \approx 1000$. From the saturation levels in the total error it is possible to obtain an estimate for the penalization error. Note that at the saturation level it can be assumed that the truncation error is no longer leading in the total error. The corresponding estimates for the penalization error are presented in Fig. 18b. The decay rate of the penalization error is consistent with the theoretical bound proportional to $\sqrt{\epsilon}$ from Carbou and Fabrie [5]. Actually the error scales slightly better, proportional to $\epsilon^{0.7}$. Note that in the simulations the asymptotic boundary layer inside the wall is not resolved properly since $\sqrt{\nu\epsilon} < 2/N$. This confirms our expectation in section (2.2) that without resolving the penalization boundary layer a $\sqrt{\epsilon}$ accuracy bound is still achievable.

Now it is possible to derive an optimal choice for the penalization parameter ϵ versus N. Recall that the minimal decay rate of the truncation error of the Fourier methods is $\delta_N = \alpha N^{-2.5}$, with constant $\alpha \approx 1.0 \times 10^4$. The penalization error scales as $\delta_\epsilon = \beta\epsilon^{0.7}$ with $\beta \approx 1$ optimum is thus achieved when $\delta_N = \delta_\epsilon$ and one readily obtains

$$\epsilon = \left(\frac{\alpha}{\beta}\right)^{10/7} N^{-3.6} \approx \gamma N^{-3.6},$$

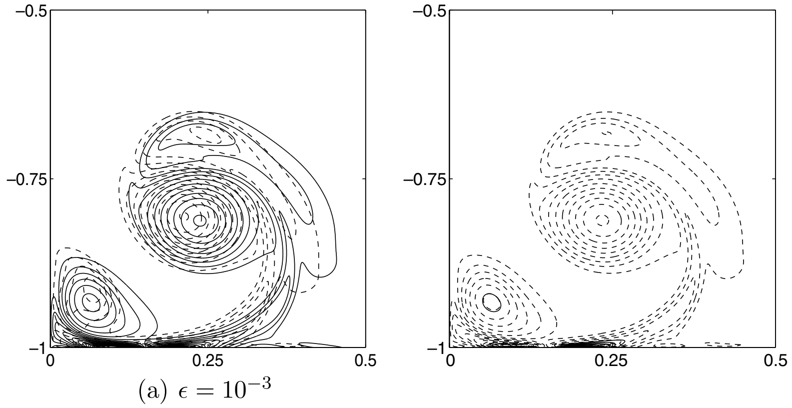

(a) $\epsilon = 10^{-3}$

Fig.17. Contour plots (dashed) of thevorticity aft

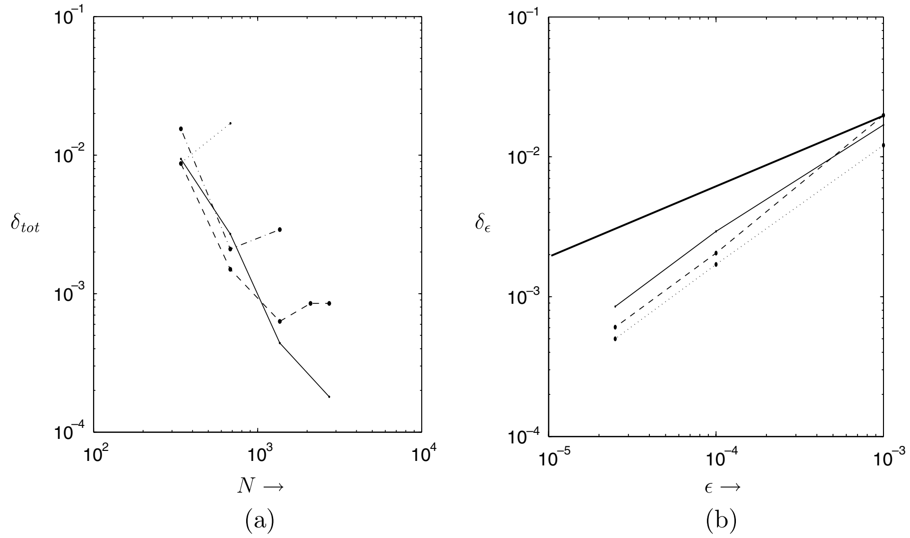

Fig. 18. Total error δ_{tot} versus number of Fourier modes N at $t = 0.8$, $\epsilon = 10^{-3}$ (dots), $\epsilon = 10^{-4}$ (dashed-dot), $\epsilon = 2.5 \times 10^{-5}$ (dashed) and $\epsilon = 10^{-8}$ (solid) (a). Modelling error versus ϵ computed at $t = 0.4$ (dots), $t = 0.5$ (dashed) and $t = 0.8$ (solid) and theoretical upper bound (b).

where γ is an $\mathcal{O}(10^5)$ constant. The same approach for the CVS method with $\delta_N = \alpha N^{-1.5}$ with $\alpha \approx 50$ yields an optimum

$$\epsilon = \left(\frac{\alpha}{\beta}\right)^{10/7} N^{-2.1} \approx \gamma N^{-2.1},$$

with γ in the order of 10^2.

9. Conclusions and discussion

Based on a difficult test case of a dipole–wall collision, we conclude that the penalized Navier–Stokes equations at high-Reynolds numbers can be solved accurately by Fourier spectral methods and coherent vortex simulation. Gibbs oscillations are present in the Fourier spectral schemes due to continuity restrictions, resulting in a poor convergence result of the truncation error. This does, however, not affect the stability such that it is not necessary to introduce any artificial viscosity terms to enhance the stability of the scheme (Ref. [18]). Furthermore, higher-order recovery of the solution can be achieved by the mollification technique proposed by Tadmor and Tanner [40]. It is very likely that similar results can be achieved by other recovery procedures like, for example, Gegenbauer postprocessing (Refs. [23,18,20]). The Petrov–Galerkin discretization used in CVS with quintic splines as a trial basis avoids the Gibbs effect such that mollification is not necessary. We found that the degrees of freedom using a grid-adaptive strategy can seriously be reduced for this particular problem, at least by a factor 1/8, without a significant loss of accuracy.

The penalization error corresponding to the difference between the solution of the penalized Navier–Stokes equations and the solution of the Navier–Stokes equations with no-slip boundary condition can be controlled by choosing appropriate values of the penalization parameter. Furthermore, the theoretical error bound of $\sqrt{\epsilon}$ obtained by Carbou and Fabrie [5] is confirmed. We found that it is not necessary to resolve the asymptotic boundary layer with a thickness proportional to $\sqrt{\nu\epsilon}$, such that an extreme refinement of the grid inside the obstacle can be avoided. This can be expected because only the order ϵ and higher order asymptotic expansions of Carbou and Fabrie [5] rely on the boundary layer solutions. For an optimal convergence scenario one has to find a balance between the truncation and penalization error. Therefore, the penalization parameter must be reduced for increasing resolutions $\epsilon \propto N^{-3.6}$. As a consequence it makes sense to decouple the time step proportional to N^{-1} from the penalization parameter. Kevlahan and Ghidaglia [24] used a GMRES

Krylov subspace technique in an explicit time-scheme for this purpose. As an alternative we propose an implicit treatment of the Darcy drag in a Fourier collocation scheme yielding good convergence results with respect to the truncation and penalization error.

Clercx and Bruneau [6] consider different important quantities of the dipole–wall collision problem, like for example the location and magnitude of the primary vortex cores, the collision time of the first and second collision, vortex-trajectories, vorticity on the wall, one-dimensional Chebyshev spectra and the pressure inside the cores of the vortices. Here, we studied the convergence in terms of the global L_2-error. It is, however, verified that convergence is achieved in terms of several of the quantities mentioned above, like the magnitude and location of both the primary and secondary vortex cores and the collision time. The computations of Clercx and Bruneau are conducted in the square bounded geometry. It is observed here that there is no significant difference between the simulations of the normal-dipole wall collision in the channel geometry or the square geometry. Clercx and Bruneau increase the initial Reynolds number $Re = 625$, 1250, 2500 and 5000. Here the Reynolds number is fixed to a moderate value of $Re = 1000$, this allows a better inspection of the asymptotic decay rate of the truncation or discretization error within a feasible range of resolutions.

In this study, we focused on the convergence of the schemes and did not address the computational aspects like, for example, the amount of CPU, memory requirements and parallelization issues. Nevertheless, some additional remarks should be made about the computational aspects of the different methods. In Table 2, the computational costs per time step are given for the Chebyshev–Fourier computation (CF), Fourier spectral scheme (FF) and the coherent vortex method (CVS). Both the Chebyshev–Fourier and Fourier spectral solver use the same FFT library and are compiled with the same compiler and optimization options. De-aliasing of the spectral methods is performed using the zero padding technique or the 2/3 rule, see Ref. [32], thus requiring larger arrays than the number of active modes. An estimate of the CPU costs presented in Table 2 is obtained by comparing the array size in the normal direction to the no-slip wall and the well-known scaling proportional to $N \log N$ of the number of operations required for the FFT, see for example Ref. [4]. Note that more FFT's are necessary in the Fourier spectral codes to incorporate volume-penalization, i.e. seven instead of five required for the Chebyshev–Fourier computations. From Table 2 it can be deduced that the actual costs per time step for the Fourier spectral method are two to three times larger due to the need for an increased array size in the wall-normal direction and extra FFT's related with the volume-penalization. The CPU-time of the CVS simulation is markedly larger. The most expensive routines are the operator adapted wavelet decompositions to solve the Helmholtz and Poisson equations, optimization of this part of the CVS code is necessary.

For a given resolution Table 2 indicates that the costs per time step are minimal for the Chebyshev–Fourier benchmark. However, the time step for the Chebyshev methods is restricted by a local CFL-condition. The strong refinement of the Gauss–Lobatto grid in the near wall region results in a stability condition

Table 2
Computational costs per time step of the Chebyshev–Fourier benchmark (CF) computation, Fourier spectral scheme (FF) and coherent vortex simulation (CVS)

Precision	$<10^{-4}$		$<10^{-3}$		
Method	CF	FF	CF	FF	CVS
N	1024	2730	384	682	1024
M	1364	1364	682	682	1024
N_{tot}	1536	4096	576	1024	1024
M_{tot}	2048	2048	1024	1024	1024
# FFT	5	7	5	7	–
FFT cost	1	4.2	1	2.7	–
CPU meas.	2.6 s	6.0 s	0.4 s	0.7 s	40 s
Memory est.	1	3	1	2	2
Memory meas. (MB)	231	750	66	105	630

CF and FF are performed on Itanium 1.3 GHz and CVS on Itanium 1.5 GHz processor. N represents the resolution in the wall normal-direction and M is resolution parallel to the wall. N_{tot} and M_{tot} denote the total array size per direction required for the computation. The FFT costs are estimated with respect to the Chebyshev–Fourier benchmark. Memory estimates are based on array size.

$\delta t \leqslant 9/M^2$ [8]. In Refs. [6,25] it is shown, on the other hand, that for higher resolutions it is possible to relax this condition somewhat. The time step for the Fourier spectral method with implicit time integration of the Darcy drag scales only linear with the number of Fourier modes. In this study the time step was fixed to a relatively small value of $\delta t = 10^{-5}$ for this comparative study. This corresponds with a CFL-number less then 0.1 for the Fourier spectral scheme, which keeps the error induced by the time scheme small with respect to the truncation error. It may be expected that substantial speed up can be gained in this respect for many practical applications while keeping the accuracy of the computation. It is anticipated that the Fourier volume-penalization algorithm will be more efficient than the Chebyshev–Fourier spectral code. We will analyze this issue in further detail in near future. Recall, that it is straightforward to compute a different geometry without additional computational requirements using volume-penalization. This is not the case for Chebyshev spectral methods. For example, the costs per time step of the Chebyshev–Chebyshev spectral method (CC) for the square geometry are substantially larger than the Chebyshev–Fourier method for the periodic channel geometry. For $N \lesssim 384$ the costs of Chebyshev–Chebyshev are proportional to $N^2 \log^2 N$, but become proportional to N^3 for $N \gtrsim 384$.

The dipole–wall collision problem can be seen as a particular problem of fully developed 2D turbulence. Accurate simulation of the collision process can reveal some important aspects, e.g. the enstrophy production on the domain boundaries [7]. It is, however, important to perform simulations of fully developed bounded turbulence, as well. For these simulations it is essential to have a high resolution in both the near-wall region and in the interior of the domain, where intensive vortex–vortex interactions require high spatial and temporal resolution. The Fourier spectral and CVS solver can benefit in this respect from the regular grids, while the number of Chebyshev modes needs to be increased substantially due to the nonregular Gauss–Lobatto grid.

In a forthcoming paper, we will present a more detailed analysis of the computational aspects involving a wider range of CFD methods like lattice-Boltzmann, finite differences and spectral elements. In addition, the potential of the Fourier and adaptive wavelet scheme will be exploited for pursuing DNS of fully developed high-Reynolds number two and three-dimensional flows in complex geometries. With respect to this purpose a promising development for CVS (see Ref. [13]) is to make the time-step adaptive in combination with adaptive multiresolution discretizations in space.

Acknowledgements

One of the authors (G.H.K.) gratefully acknowledges financial support from the Dutch Foundation for Fundamental Research on Matter (FOM). This work was sponsored by the Stichting Nationale Computerfaciliteiten (National Computing Facilities Foundation, NCF) for the use of supercomputer facilities, with financial support from the Nederlandse Organisatie voor Wetenschappelijk Onderzoek (Netherlands Organisation for Scientific Research, NWO). U.O. and K.S. thankfully acknowledge financial support from the Agence Nationale de la Recherche, ANR contract M2TFP.

References

[1] P. Angot, C.-H. Bruneau, P. Fabrie, A penalization method to take into account obstacles in viscous flows, Numer. Math. 81 (1999) 497.

[2] E. Arquis, J.P. Caltagirone, Sur les conditions hydrodynamique au voisinage d'une interface milieu fluide-milieu poreux: application à la convection naturelle, C.R. Acad. Sci. Paris 299 (Série II) (1984) 1–4.

[3] C. Beta, K. Schneider, M. Farge, Wavelet filtering to study mixing in 2D isotropic turbulence, Commun. Nonlinear Sci. Numer. Simulat. 8 (2003) 537.

[4] C. Canuto, M.Y. Hussaini, A. Quarteroni, T.A. Zang, Spectral Methods in Fluid Dynamics, Springer-Verlag, Berlin, 1987.

[5] G. Carbou, P. Fabrie, Boundary layer for a penalization method for viscous incompressible flow, Adv. Differ. Equat. 8 (2003) 1453.

[6] H.J.H. Clercx, C.-H Bruneau, The normal and oblique collision of a dipole with a no-slip boundary, Comput. Fluids 35 (2006) 245.

[7] H.J.H. Clercx, G.J.F. van Heijst, Dissipation of kinetic energy in two-dimensional bounded flows, Phys. Rev. E 65 (2002) 066305.

[8] H.J.H. Clercx, A spectral solver for the Navier–Stokes equations in the velocity–vorticity formulation for flows with two non-periodic direction, J. Comput. Phys. 137 (1997) 186.

[9] H.J.H. Clercx, A.H. Nielsen, D.J. Torres, E.A. Coutsias, Two-dimensional turbulence in square and circular domains with no-slip walls, Eur. J. Mech. B-Fluid. 20 (2001) 557.

[10] G-H Cottet, P. Koumoutsakos, M.L. Ould-Salihi, Spatially varying cores for viscous vortex methods, J. Comput. Phys. 162 (2000) 164.

[11] G-H Cottet, P. Koumoutsakos, Vortex Methods: Theory and Practice, Cambridge University Press, Cambridge, 2000.

[12] O. Daube, Resolution of the 2D Navier–Stokes equations in velocity–vorticity form by means of an influence matrix technique, J. Comput. Phys. 103 (1992) 402.

[13] M. Domingues, O. Roussel, K. Schneider, On space: time adaptive schemes for the numerical solution of partial differential equations, ESAIM Proc. 16 (2007) 181.

[14] W.S. Don, Numerical study of pseudospectral methods in shock wave applications, J. Comput. Phys. 110 (1994) 103.

[15] M. Farge, K. Schneider, N.K.R. Kevlahan, Non-Gaussianity and coherent vortex simulation for two-dimensional turbulence using an adaptive orthogonal wavelet basis, Phys. Fluids 11 (1999) 2187.

[16] M. Farge, K. Schneider, Coherent vortex simulation (CVS) a semi-deterministic turbulence model using wavelets, Flow. Turbul. Combust. 66 (2001) 393.

[17] J. Fröhlich, K. Schneider, An adaptive wavelet–vaguelette algorithm for the solution of PDEs, J. Comput. Phys. 130 (1997) 174.

[18] D. Gottlieb, S. Gottlieb, Spectral methods for discontinuous problems, in: D.F. Griffiths, G.A. Watson (Eds.), Proceedings of the 20th Biennial Conference on Numerical Analysis, University of Dundee, 2003, p. 65.

[19] D. Gottlieb, E. Tadmor, Recovering pointwise values of discontinuous data within spectral accuracy, in: E.M. Murman, S.S. Abarbanel (Eds.), Proceedings of the Progress and Supercomputing in Computational Fluid Dynamics, vol. 6, 1984, Progress in Science Computing (Birkhauser, Boston, 1985) p. 357.

[20] D. Gottlieb, C.-W Shu, General theory for the resolution of the Gibbs phenomenon, Accademia Nazionale Dei Lincei, ATTI Dei Convegni Lincei 147 (1998) 39.

[21] D. Gottlieb, C.-W. Shu, A. Solomonoff, H. Vandeven, On the Gibbs phenomenon I: recovering exponential accuracy from the Fourier partial sum of a nonperiodic analytic function, J. Comput. Appl. Math. 43 (1992) 81.

[22] E. Hairer, S.P. Nørsett, G. Wanner, Solving Ordinary Differential Equations II in Stiff and Differential-Algebraic Problems, 2nd ed., Springer-Verlag, Berlin, 1996.

[23] J.H. Jung, B.D. Shizgal, Generalization of the inverse polynomial reconstruction method in the resolution of the Gibbs phenomenon, J. Comput. Appl. Math. 172 (2004) 131.

[24] N.K.R. Kevlahan, J.-M. Ghidaglia, Computation of turbulent flow past an array of cylinders using spectral method with Brinkman penalization, Eur. J. Mech. B-Fluid. 20 (2001) 333.

[25] W. Kramer, Dispersion of tracers in two-dimensional bounded turbulence, Ph.D. thesis, Eindhoven University of Technology, The Netherlands, 2007.

[26] A.G. Kravchenko, P. Moin, R. Moser, Zonal embedded grids for numerical simulation of wall-bounded turbulent flows, J. Comput. Phys. 127 (1996) 412.

[27] W. Kress, P. Lötstedt, Time step restrictions using semi-explicit methods for the incompressible Navier–Stokes equations, Comput. Method. Appl. M. 195 (2006) 4433.

[28] P.D. Lax, Accuracy and resolution in the computation of solutions of linear and nonlinear equations, in: Proceedings of the Recent Advances in Numerical Analysis Mathematical Research Center, University of Winsconsin, Academic Press, 1978, p. 107.

[29] A. Madja, J. McDonough, S. Osher, The Fourier method for nonsmooth initial data, Math. Comput. 32 (1978) 1041.

[30] P. Orlandi, Vortex dipole rebound from a wall, Phys. Fluids A 2 (1990) 1429.

[31] M.L. Ould-Salihi, G-H Cottet, M. El Hamraoui, Blending finite-difference vortex methods for incompressible flow computations, J. Sci. Comput. 22 (2000) 1655.

[32] S.A. Orszag, Numerical methods for the simulation of turbulence, Phys. Fluids 12 (Suppl. II) (1969) 250.

[33] A. Paccou, G. Chiavassa, J. Liandrat, K. Schneider, A penalization method applied to the wave equation, C.R. Mécanique 333 (2005) 79.

[34] K. Schneider, The numerical simulation of transient flow behaviour in chemical reactors using a penalization method, Comput. Fluids 34 (2005) 1223.

[35] K. Schneider, M. Farge, Coherent vortex simulation (CVS) of dipole–wall interaction using volume penalization, in: Advances in Turbulence X, Proceedings of the Tenth European Turbulence Conference, 2004, p. 621.

[36] K. Schneider, M. Farge, Adaptive wavelet simulation of a flow around an impulsively started cylinder using penalisation, Appl. Comput. Harmon. A 12 (2002) 374.

[37] K. Schneider, M. Farge, Numerical simulation of temporally growing mixing layer in an adaptive wavelet basis, C.R. Acad. Sci. Paris Série II b 328 (2000) 263.

[38] K. Schneider, M. Farge, G. Pellegrino, M. Rogers, Coherent vortex simulation of three-dimensional turbulent mixing layers using orthogonal wavelets, J. Fluid Mech. 534 (2005) 39.

[39] C.-W. Shu, P. Wong, A note on the accuracy of spectral methods applied to nonlinear conservation laws, J. Sci. Comput. 10 (1995) 357.

[40] E. Tadmor, J. Tanner, Adaptive mollifiers for high resolution recovery of piecewise smooth data from its spectral information, Found. Comput. Math. 2 (2002) 155.

[41] Z. Yin, H.J.H. Clercx, D.C. Montgomery, On an easily implemented parallel scheme for a 2D Fourier pseudospectral algorithm, Comp. Fluids 33 (2004) 509.